

Full length article

The effects of synthesis route and LaB₆-doping on FeCoNiCrTi coating performance: Morphology, microstructure, microhardness and corrosion resistance

Dadong Jie ^{a,c}, Meiping Wu ^{a,c}, Rui He ^{a,c}, Chen Cui ^{a,c}, Yuling Gong ^{a,b}, Xiaojin Miao ^{a,c,*}

^a College of Mechanical Engineering, Jiangnan University, Wuxi 214122, China

^b School of Shipping and Mechatronic Engineering, Taizhou University, 225300 Taizhou, China

^c Jiangsu Key Lab Adv Food Mfg Equipment & Technol, Wuxi 214122, China



ARTICLE INFO

ABSTRACT

Keywords:

High entropy alloy
Laser energy density
LaB₆
Laser cladding
Microhardness and corrosion resistance

In this work, the FeCoNiCrTi HEA coatings were fabricated on the Ti6Al4V surface via laser cladding technology. The effects of synthesis routes (different energy density, L_{ed}) and LaB₆-doping on the single-track morphology, phase distribution, microstructure, microhardness and corrosion resistance of HEA coatings were comprehensively studied. Interestingly, the regulation of L_{ed} and addition of LaB₆ significantly reduced the crack sensitivity and dilution rate of the coating. On the one hand, the optimized coating contributed to fine grain size when L_{ed} was 73.33 J/mm². On the other hand, the in-situ generation of TiC, TiB₂ and TiC/TiB₂ composite structure played an important role in achieving the more excellent property in LaB₆/FeCoNiCrTi composite coating. Furthermore, the microhardness and corrosion resistance of the coatings were significantly improved owing to the ceramic phases and fine grain strengthening. Specifically, the average microhardness coating was up to 593 HV_{0.2}. The corrosion current density (I_{corr}) of the coating with a L_{ed} of 73.33 J/mm² was 4.796×10^{-6} A·cm⁻², the carrier density (N_D) and thickness (d) of the passivation film were 1.556×10^{22} cm⁻² and 3.244 nm, respectively, indicating the best corrosion resistance in HEA coatings. In terms of LaB₆/FeCoNiCrTi coating, the I_{corr} , N_D and d were 2.400×10^{-6} A·cm⁻², 1.053×10^{22} cm⁻² and 4.739 nm, respectively. Consequently, the doping of LaB₆ further enhanced the corrosion resistance of HEA coating.

1. Introduction

Ti6Al4V, as an excellent engineering material, is widely used in key components such as steam turbine blades because of its high specific strength, good corrosion resistance, and strong fatigue performance [1,2]. Unfortunately, the Ti6Al4V had low hardness [3], making it difficult to overcome the coupling environment of high load and corrosion which severely limits the lifespan of the blades. Thus, how to improve the surface hardness and corrosion resistance of titanium alloys has become a research hotspot.

Over the past two decades, the fabrication of metal coatings has been proven to be an effective method for improving the properties of material surface [4]. Noticeably, the coating properties depend on the coating material and preparation process. In terms of materials, high entropy alloys (HEAs) have become attractive metal coating materials owing to their excellent mechanical and corrosion resistance [5,6]. For

the fabrication technology, laser cladding (LC), as an emerging material deposition technology [7], can deposit coatings ranging from 0.2 to 2 mm on alloy surfaces. Compared with traditional technologies, LC keeps the characteristics of fast cooling speed, low dilution rate, and small thermal deformation [8,9]. Therefore, fabricating the HEA coatings by LC to enhance hardness and corrosion resistance of Ti6Al4V is undoubtedly an effective strategy.

Noticeably, the forming quality and properties of coatings depend on whether the composition of HEAs and LC process route is reasonable. On the one hand, the “cocktail effect” [10] promotes various elements to obtain a composite effect on the properties of HEAs. Consequently, the particular properties can be achieved by adding particular elements. For instance, the Cr and Ni elements for corrosion resistance, and Ti elements for enhanced hardness. Furthermore, HEAs considering the 3d-transitional-element (Co, Cr, Fe, Ni, Mo, Ti, etc.) as the base constituent can obtain simple solid solution easily (FCC or BCC) [11,12], which

* Corresponding authors at: College of Mechanical Engineering, Jiangnan University, Wuxi 214122, China.

E-mail addresses: wumeiping163@163.com (M. Wu), miaoxiaojin126@126.com (X. Miao).

promoted high hardness [13,14] and high corrosion resistance [15,16]. It is worth mentioning that the FeCoNiCrMo coating successfully prepared by our team in the early stage confirmed the above conclusions [17]. However, considering that the substrate is Ti6Al4V, the Mo element is replaced by Ti in this work to improve the chemical compatibility between the powder and the substrate. Thus, this work chose the FeCoNiCrTi HEAs as the coating material. On the other hand, better controlling of process variables is crucial to achieve specific properties in any material science experiment [18]. In this connection, many scholars [19,20] have researched on the effect of laser processing variables on coating properties, confirming that laser energy density (L_{ed}) is a critical processing feature that affects the morphology, microstructure, and properties of coatings.

Unfortunately, the single solid solution was prone to embrittlement [21]. In addition, HEAs does not match the thermal expansion of the substrate at high temperature, which makes coating prone to crack initiation [22,23]. According to reports, refining the microstructure is an effective method to reduce the cracking sensitivity of coatings [24]. Additionally, rare earth elements have attracted much attention owing to the special electronic structure and outstanding chemical activity, and have been proved to be effective in providing more nucleation cores for grain refinement during LC [25]. In recent years, relevant scholars [26,27] have successfully enhanced coatings on titanium alloys by

adding rare earth elements. The types of Re are mostly concentrated in such as Ce, La, and Y. Especially, for the attempt of La, Feng et al. [28] added different amount of LaB₆ to the (Ti3Al + TiB)/Ti composite material prepared on Ti6Al4V by LC. The results showed that the microstructure of the composite coating (2 wt% LaB₆) was refined, and the properties (hardness, wear resistance, and high-temperature oxidation resistance) were significantly improved. It is due to the more prominent advantage of LaB₆ compared to other rare earths when mixed with Ti. Specifically, it can promote the in-situ generation of TiB₂ and TiB, further refining the grains and strengthening the mechanical properties of the coating [29,30]. Accordingly, the introduction of a certain amount of LaB₆ is expected to further improve the forming quality and properties of the substrate (Ti6Al4V) and cladding materials (FeCoNiCrTi) in this work.

In summary, this work aimed to improve the microhardness and corrosion resistance of Ti6Al4V and explored the influence of L_{ed} on the morphology, microstructure, corrosion behavior and microhardness of the HEA coatings. Based on previous publications [17] and Liang's work [31], 2 wt% LaB₆ particles were introduced into the self-designed FeCoNiCrTi powder, and LaB₆/FeCoNiCrTi composite coating was fabricated successfully via LC under the optimal laser process parameters of C1-C4. Eventually, the strengthening mechanism of LaB₆ on the composite coating properties was analyzed.

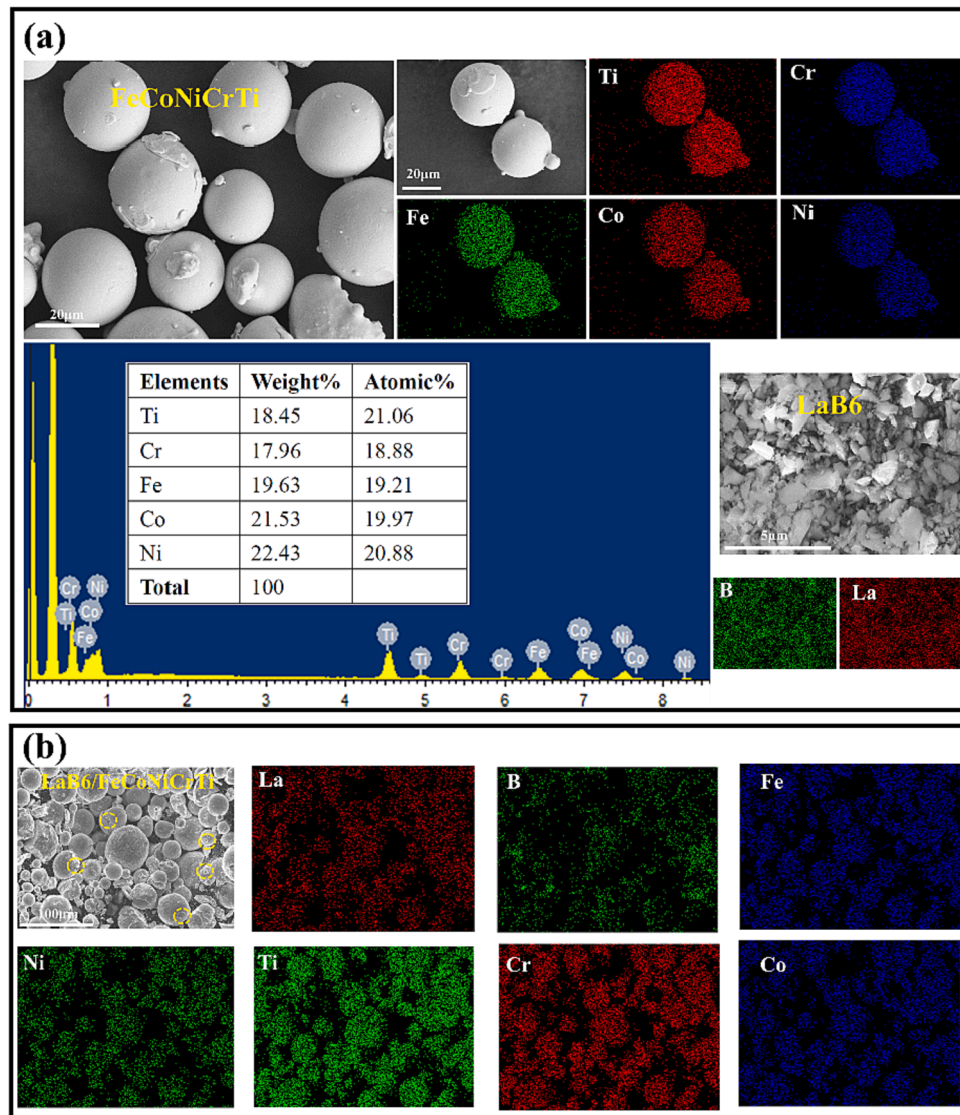


Fig. 1. SEM images and EDS results of powders: (a) FeCoNiCrTi and LaB₆; (b) 98wt.%FeCoNiCrTi + 2 wt% LaB₆.

2. Experiment procedures and numerical simulation

2.1. Materials

The bulk Ti6Al4V (the size is 120 mm × 10 mm × 8 mm) was selected as the substrate for this work. The chemical composition (wt.%) of the Ti6Al4V alloy is Al 6.03, V 4.01, C 0.1, Fe 0.3, N 0.02, O 0.05, and Ti (bal.). Coating powder was commercially FeCoNiCrTi high-entropy alloy powders (Gaoke new materials Co., Ltd, China). The size of FeCoNiCrTi powders was 15–53 µm and its chemical composition are shown in Fig. 1(a). Additionally, the reinforcing particles selected the LaB₆ with 99.9 % purity and a size of 5–10 µm. To fabricate a better quality composite coating, it was necessary to mix LaB₆ (2 wt%) and FeCoNiCrTi (98 wt%) powder homogeneously. The powders were put into the planetary ball mill (China Nanda Technology Co., Ltd.) for 2 h at the speed of 300 rpm. The weight ratio of powder to ball was 1:2. To eliminate the influence of thermal energy generated by high-energy ball milling on the composite powder, the machine was supposed to shut down for 5 min every 15 min and reversed the direction of the ball mill. The SEM images of LaB₆ powders and LaB₆/FeCoNiCrTi composite powders are shown in Fig. 1(b). It could be seen that the powder mixing effect is very satisfactory.

2.2. Coating preparation

HEAs coatings were prepared by coaxial powder feeding laser cladding equipment (Nanjing Pfizer Optoelectronic Technology Co., Ltd.). The equipment was composed of fiber laser, platform, powder feeder system and laser head, as shown in Fig. 2(a). To remove the oxides and contaminants on the surface of Ti6Al4V, the surface was polished by grinding machine with abrasive paper (#80 SiC sandpapers) before the cladding experiment. And it was cleaned with acetone. Furthermore, the mixed powders was dried in a vacuum drying for 2 h at 100 °C. In order

to explore the impact of L_{ed} on the formability quality and performance of coating, four different L_{ed} process routes were set up, as shown in Table 1. The L_{ed} can be defined by the following formula [32]:

$$L_{ed} = \frac{P}{V \times D} \quad (1)$$

where P denotes the laser power, V denotes the scanning speed, D denotes the spot diameter. $L_{ed} = 44 \text{ J} \cdot \text{mm}^{-2}$, $55 \text{ J} \cdot \text{mm}^{-2}$, $73.33 \text{ J} \cdot \text{mm}^{-2}$, $80.0 \text{ J} \cdot \text{mm}^{-2}$ were designated as C1, C2, C3, C4 respectively. C5 represents the LaB₆ / FeCoNiCrTi composite coating prepared under the optimal process parameters of C1–C4.

2.3. Numerical model

To better understand the heat transfer, molten flow and solidification behavior during the preparation of HEAs coating via LC, a coupled multi-physics field numerical model was established. In consideration of the calculation time cost, the symmetric boundary condition was adopted to improve calculation efficiency (a half the width), as shown in Fig. 3. The size of the substrate selected for calculation was 15 mm × 10 mm × 4 mm in length, width and height, respectively. Additionally, the computational domain was divided into two parts by tetrahedral elements, in which region I adopted refined grid elements and region II adopted coarser grid elements. Specifically, the minimum size of the grids was 0.003 mm and computational degrees of freedom was 429505. The molten pool evolution was a highly transient process in LC. Some necessary assumptions were proposed in order to make the problem mathematically tractable, including: (1) all powders entering the molten pool were involved in the formation of the coating; (2) the heat flux of the heated powder and the heat loss by evaporation were neglected; (3) the fluid flow in the molten pool was assumed to be incompressible, Newtonian and laminar; (4) the influence of buoyancy, the influence of evaporation recoil pressure and the influence of air resistance caused by shielding gas were not considered. Simultaneously, the other model information including thermophysical parameters of materials, boundary conditions and governing equations could be found in our previous work [33], which were not repeated here.

2.4. Characterization

In this work, the geometric morphology, XRD, and microstructure of the coating was characterized. Single-track cladding coatings with dimensions of 10 mm × 10 mm × 6 mm were cut along cladding direction by a wire-EDW machine for experimental characterization. The cross-section of the coatings were polished with sandpaper of different roughness (800-, 1500-, 2000-, 2500-mesh sandpapers), then polished by polishing cloth with polishing paste, which finally were rinsed with anhydrous ethanol. To observe the organization, it was necessary to use aqua regia ($\text{HNO}_3:\text{HCl} = 1:3$, Vol%) to etch the polished section. The microstructure and geometric morphology of C1–C5 were observed by a scanning electron microscope (SEM, SIGMA HD, Germany) equipped with an energy dispersive spectrometer (EDS, 51-XMX1003, Germany). The phase composition of C1–C5 coatings was characterized by an X-ray

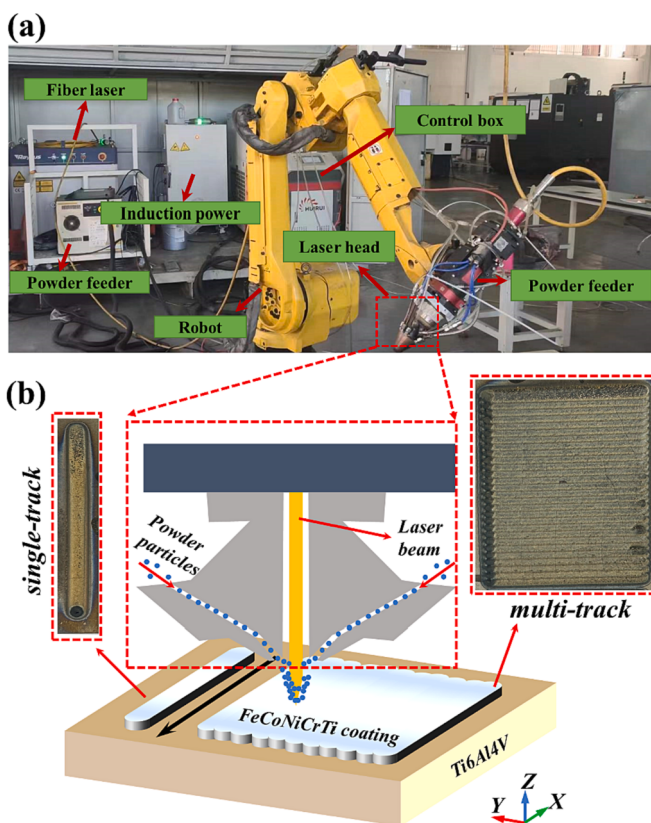


Fig. 2. Schematic diagram of laser cladding process.

Table 1
The parameters for the laser cladding process.

Samples	P (W)	V (mm/min)	D (mm)	L_{ed} (J·mm ⁻²)	m_f (g/min)	Powders
C1	2200	600	5	44.0	18	100wt.% FeCoNiCrTi
C2	2200		4	55.0		
C3	2200		3	73.33		
C4	2400		3	80.0		
C5	2200		3	73.33		98wt.% FeCoNiCrTi + 2wt.%LaB ₆

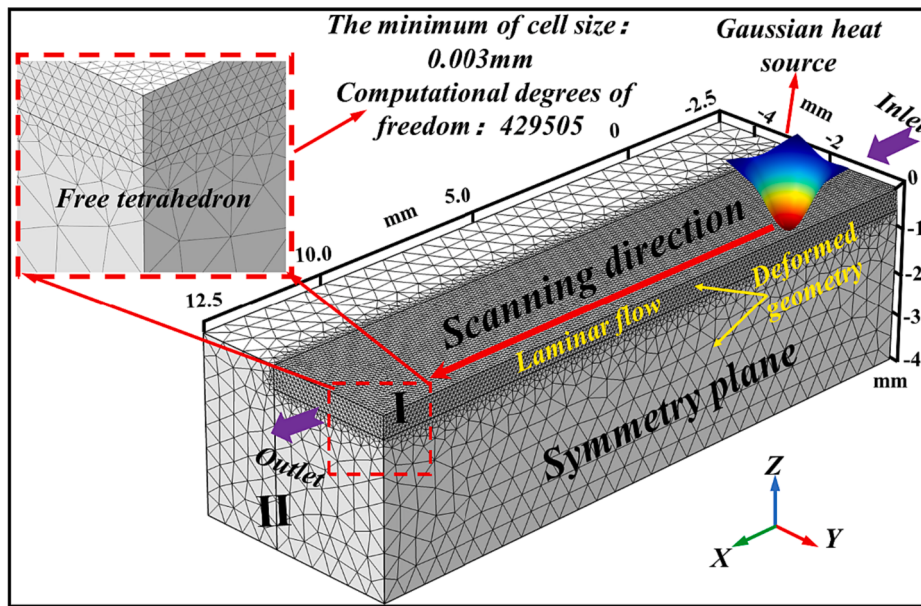


Fig. 3. The establishment of numerical simulation.

diffraction (XRD-D8, Germany) with Cu K α radiation, and the working voltage and current were 4 kV and 30 mA, respectively.

2.5. Microhardness and corrosion resistance

The microhardness of C1–4 were measured by a Vickers microhardness tester (HVS-1000ZCM-XY, China) with a load of 200 g and a holding time of 30 s. To explore the microhardness changes of coatings and substrate, the gradient microhardness points were set from the top of HEA coating to the substrate. To ensure the reliability of the test results, each sample was measured three times to obtain the average microhardness.

Before the experiment, the multi-track coatings were cut into the size of 10 mm × 10 mm × 3 mm for the convenience of testing the corrosion resistance, and then the samples were wrapped with insulating glue except for the coating. In this experiment, Ag/AgCl was selected as the reference electrode, the coating samples were the working electrode and the platinum sheet was auxiliary electrode. The corrosion testing of coating samples were conducted by using an electrochemical workstation (CHI750E, USA) at room temperature ($20^\circ\text{C} \pm 3^\circ\text{C}$) and an electrolyte of 3.5 wt% NaCl solution. The measurement range of the potentiodynamic polarization curve was -1 V – 1.6 V at a scan rate of 0.001 V/s. Furthermore, it was necessary to wait for the open circuit potential (OCP) to stabilize for 2000 s before measuring the electrochemical impedance spectroscopy (EIS). At last, the data of EIS was fitted by commercial software ZSimpWin.

3. Results and discussion

3.1. Crack sensitivity and geometric characteristics

In terms of cracks generation, the formation process of coatings inevitably generated stress owing to the rapid melting and cooling of LC, including thermal stress, residual stress, constraint stress, etc. The stress made the coatings prone to crack sensitivity. Commonly, there were three most likely cracking types in the LC process, i.e. solidification cracking, liquation cracking and ductility-dip cracking [34]. In particular, solidification cracking occurred in the last period of solidification when thermal stress was accumulated sufficiently between dendrites [35]. It can be seen that the cracks initiated from the fusion line and extend to the coating surface in the intergranular form, as shown in

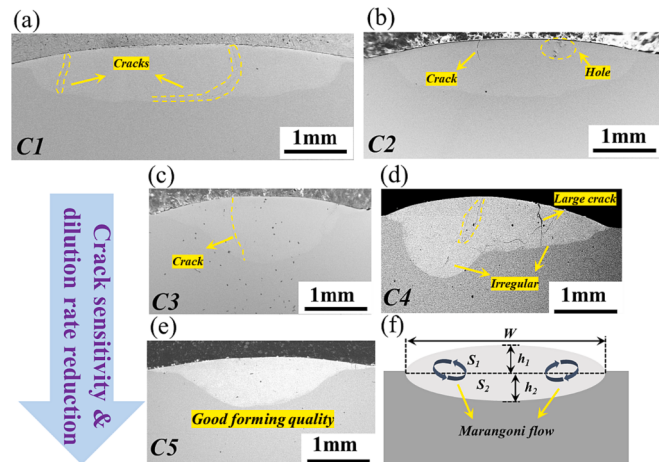


Fig. 4. (a–e): The cross-sectional morphologies of single-track of C1–C5; (f) the mechanism diagram of geometric characteristic.

Fig. 4. Therefore, the defects of this work were typical solidification cracks in the coatings. The thermal stress played a dominant role in the generation of solidification cracks, and was positively related to the difference between the thermal expansion coefficient of the coating and the substrate [36]. Noticeably, the thermal expansion coefficient of FeCoNiCr HEA system was higher than Ti6Al4V. Consequently, the thermal stress of the coating was tensile stress.

Generally, the morphology of the single-track coatings preliminarily determined the quality of coating formation under different processes. Fig. 4(a–e) shows the cross-sectional morphologies of C1, C2, C3, C4, C5 single-track. It was found that C1–C4 coatings exhibit different types and quantities of defects. Noticeably, the number of defects firstly decreased and then increased as the increase of the L_{ed} . Especially, the C4 exhibited more defects which were huge. Furthermore, the excessive defects lead to uneven energy distribution in the preparation process of C4 coating, resulting in the irregular forming morphology as shown in Fig. 4(d). Accordingly, appropriate energy density could effectively reduce the defects of coatings.

The main reasons could be analyzed from both macro and micro perspectives. From a macro perspective, the thermal input of the coating

increased as the L_{ed} increased. On the one hand, the decrease in the number of intervals between the dissolved and undissolved particles in the coating reduced the sensitivity to cracking, which was manifested in a gradual decrease in the number, length, and width of cracks on a macroscopic level. On the other hand, the retention time and fluidity of the molten pool were enhanced with the increase of heat input. The gas and unmelted particles floated up to the coating surface for a long time, which reduced pores and impurities in the coating. It meant that the source of cracks decreased which inhibited the tendency for the cracks of coatings. Unfortunately, the Marangoni convection effect was enhanced when the laser energy density was too high. The gas, which entrained in the powder, was easily trapped in the coating and dragged to be retained. Hence, the defects increased in the C4. From a microscopic perspective, a suitable L_{ed} made the HEA elements more fully mixed and enhanced the metallurgical bonding with the matrix. In addition, the coating microstructure was refined (as described later in the microstructure analysis), thereby reducing the tendency for cracking.

Obviously, the C5 coating did not show any obvious defects, as shown in Fig. 4(e). Accordingly, the addition of quantitative LaB₆ had a positive effect on inhibiting crack initiation. The effectiveness of LaB₆ in suppressing cracks was mainly attributed to the following reasons: (1) The addition of LaB₆ increased the absorption rate of the powders, which allowed more matrix elements to be incorporated into the mushy area, thereby narrowing the gap between the thermal properties of the coating material (FeCoNiCrTi) and the matrix (Ti6Al4V). (2) LaB₆ particles remained at the front of the solidification interface, which was beneficial for removing unmelted materials and intercepting bubbles [37]. Hence, the tendency to form cracks was reduced in the coating. (3) LaB₆ reacted in situ with Ti element to generate the TiB_x phase which refined the microstructure, and the toughness of the coating increased. Simultaneously, the TiB_x phase absorbed and dispersed stress, thereby reducing the concentration and propagation of cracks. The viewpoint was conspicuously validated in the C5 coating cross-section.

In addition, the shape of the C1-C5 coatings were elliptical, which was attributed to the Marangoni effect in the molten pool. Generally, the distribution of laser heat sources was approximately Gaussian, resulting in an uneven distribution of energy in the molten pool [38]. The uneven energy promoted a large temperature gradient and surface tension in the molten pool, thereby driving the molten pool to flow to both sides at

lower temperature. Ultimately, the vortices, known as Marangoni convection, grow up on both sides of the molten pool with a laser beam as the axis of symmetry, as shown in Fig. 4(f). Noticeably, the geometric characteristics of the coatings significantly changed owing to the intensity of Marangoni convection. The intensity of Marangoni convection was expressed by the Marangoni coefficient (M_a) [39].

$$M_a = \frac{|\gamma| L_R \Delta T_r}{\mu \eta} \quad (2)$$

where γ denotes the temperature coefficient of surface tension, ΔT_r denotes the maximum temperature difference in the molten pool, L_R denotes the length of the molten pool, μ denotes the dynamic viscosity of the molten pool, and η denotes the thermal diffusivity. Fig. 5 shows the simulated convection velocity and geometry of the molten pool. Among them, the maximum convection velocity of C1-C4 were 0.42 m/s, 0.50 m/s, 0.75 m/s and 0.85 m/s, respectively. Both the L_R and convection velocity, which determined the convective mixing time of the melt pool, increased with the L_{ed} . The increase of convective time was beneficial for improving the homogeneity of components in the molten pool, which reduced the element concentration gradient inside the coating. Large element concentration gradients often lead to significant differences in thermal expansion and wettability of the coatings, making it easy to form cracks. Accordingly, properly increasing the L_{ed} could reduce the crack sensitivity of the coating, which was consistent with the previous analysis.

The geometry of the coating is one of the criteria for assessing the coating quality [40]. Fig. 4(f) displays the geometric characteristic parameters of the coating, mainly including width (W), height (h_1), depth (h_2), the area of the upper part of the (S_1) and the area of the under part of the coating (S_2). Moreover, based on the above characteristic parameters, the indicator that effectively reflect the interface between the coating and the substrate were obtained, namely dilution rate (η). The η of the single-track coatings was calculated according to the following formula [41]:

$$\eta = \frac{S_2}{S_1 + S_2} \times 100\% \quad (3)$$

To explore the influence of process routes on the coatings geometric, the geometric characteristics of C1-5 coatings were measured by Image-

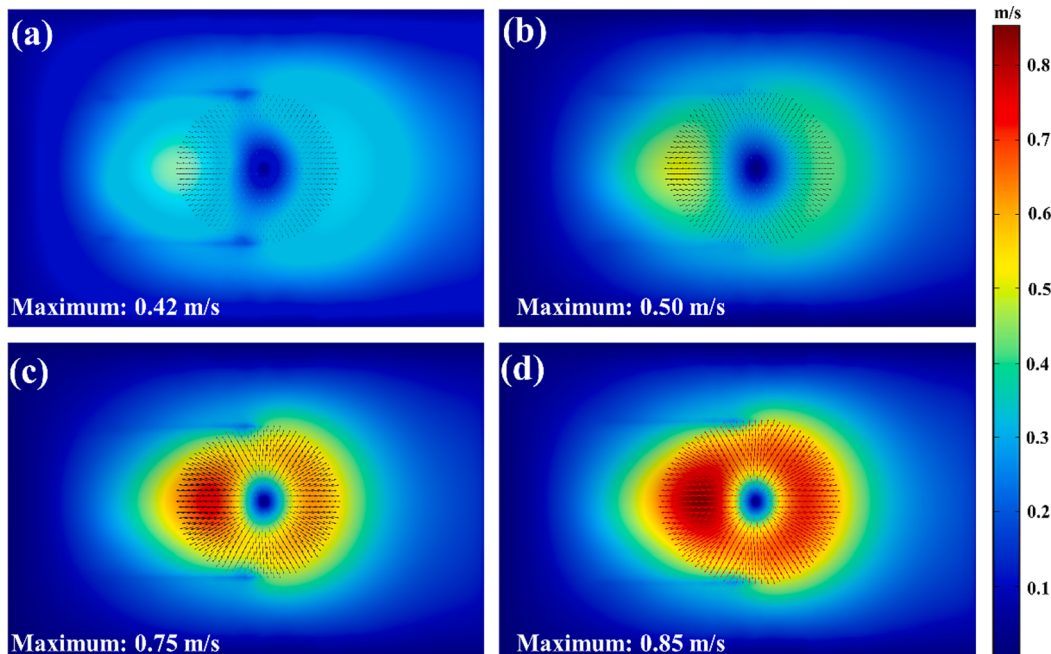


Fig. 5. Distribution diagram of molten pool velocity for different samples at 0.5 s: (a) C1; (b) C2; (c) C3; (d) C4.

Pro software. **Table 2** displays the specific values of geometric characteristics. It could be found that the coatings width was significantly positively correlated with the diameter of the spot diameter (D), which was consistent with the findings of Hofman et al. [42]. The W was greater than D because the Marangoni convection allowed the metal liquid to flow to both sides. Moreover, the effect of L_{ed} on h_2 was significantly greater than that on h_1 , which was attributed to the fact that the h_1 mainly depended on the powder feeding rate [43]. The increase of L_{ed} enabled more material to melt, thus creating a deeper molten pool. The η of C1-C5 were calculated by using Eq. (3), as shown in **Fig. 6**. The deeper the coating penetration as the L_{ed} increased, and the higher the dilution rate. However, there was an abnormal situation with the C4 coating owing to the irregular forming morphology. Additionally, Wang et al. [44] demonstrated that rare earth phases increased the melting latent heat of the alloy, which promoted an increase of solidus temperature and a decrease of liquidus temperature. Ultimately, the solidification time and range of the coatings were reduced, effectively reducing the η of the coating. The η of C5 coating was 60.18 %, which was a strong proof of that.

3.2. Phase analysis

Fig. 7(a) shows the phase composition of the FeCoNiCrTi HEA coatings under different L_{ed} and LaB₆/FeCoNiCrTi composite coating. The main diffraction peak angles of C1–C4 coatings indicated that the phase compositions of FeCoNiCrTi HEA coating were BCC solid-solution phase and Ti₂Ni. The formation of BCC phase was attributed to the mixing enthalpy approximation of Fe, Co, Ni, Cr, which played a leading role in the phase composition [45]. To be more specific, the phase composition of HEA coatings which were prepared under different L_{ed} did not change, but the relative strength changed. In addition, it could be observed that the peak location of BCC phase moved towards the smaller 2θ as the L_{ed} increased. This phenomenon could be explained as more substrate material (Ti6Al4V) dissolved into the molten pool, which promoted more Ti elements to enter the molten pool. The large atomic radius of Ti was, the greater atomic radius difference was in the coating, theybe the XRD peak moved to the left.

With the rapid movement of the laser beam, the solidification of the molten pool promoted the complex physical and chemical reactions. Especially, the ceramic particle phase (TiB_x and TiC) were observed in C5 coating when the LaB₆ was added. According to the analysis results of XRD and thermodynamic calculations [46] (**Fig. 7(b)**), the following reactions occurred during the solidification process of the molten pool:

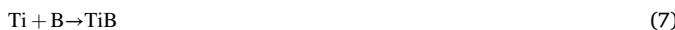


Table 2
The geometry characteristics of C1-C5 coatings.

Samples	W (mm)	h_1 (mm)	h_2 (mm)	S_2 (mm ²)	$S_1 + S_2$ (mm ²)
C1	5.252 ± 0.080	0.319 ± 0.043	0.540 ± 0.058	2.389 ± 0.043	3.511 ± 0.022
C2	4.267 ± 0.076	0.309 ± 0.061	0.587 ± 0.072	1.836 ± 0.035	2.672 ± 0.012
C3	3.230 ± 0.024	0.285 ± 0.028	0.742 ± 0.067	1.320 ± 0.032	1.903 ± 0.020
C4	3.304 ± 0.086	0.380 ± 0.055	0.864 ± 0.091	1.520 ± 0.039	2.419 ± 0.031
C5	3.398 ± 0.528	0.190 ± 0.011	0.544 ± 0.066	0.633 ± 0.016	1.052 ± 0.035

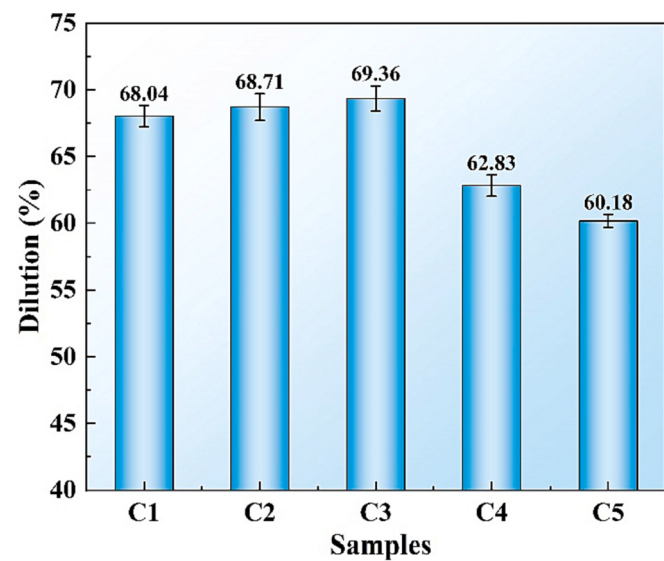
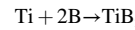


Fig. 6. Dilution of single-track C1–5.



The data showed very clearly that the ΔG values of all reactions were less than 0, indicating that all reactions spontaneously generated. Moreover, the TiNi preferentially precipitated during the solidification process of the molten pool. However, the TiNi was unstable, which reacted with Ti to generate Ti₂Ni (peritectic reaction). It was worth mentioning that the Ti₂Ni phase exhibited strong phase structure stability in Ti-Ni binary alloy system [47]. Noticeably, the high melting points and low ΔG value of TiB₂ and TiC promoted the preferential precipitation of TiB₂ and TiC. Simultaneously, the ΔG of TiB₂ was less than the TiC, which meant that required less undercooling value. Hence, the pre-precipitated TiB₂ generated a heterogeneous nuclei effect on TiC to cultivate a eutectic structure of TiC/TiB₂, which significantly influenced the properties of the coating.

3.3. Dynamic solidification behavior and microstructure

Fig. 8(a) shows the simulated temperature distribution under the same process parameters as C3 coating at 200 ms. The result showed very clearly that the temperature of the spot center was 3.61×10^3 K, which has exceeded the solidus temperature of the substrate material [48]. The substrate began to melt and eventually an elliptical shaped molten pool was formed. With the influence of heat conduction, there existed a preheating transition zone between the coating area and the area without coating. To better investigate the development of coating the temperature distribution of the molten pool section ($X = 2$ mm) at different times is calculated, as shown in the **Fig. 8(b)**. During the melting stage (120 ms–200 ms), the powder was continuously injected into the molten pool, causing protrusions and temperature rise of the coating as the spot approached. When the spot left the position of the cross-section, the molten pool began to enter the solidification stage (280 ms–360 ms) and the coating height no longer changed, indicating that the coating was fully developed [49].

Related researches [50,51] shown that the type and size of grains depended on solidification parameters, including temperature gradient (G) and solidification rate (R). The G and R was calculated as follows [52]:

$$G = \frac{2\pi K(T_L - T_0)^2}{Q} \quad (9)$$

$$R = VC \cos \alpha \quad (10)$$

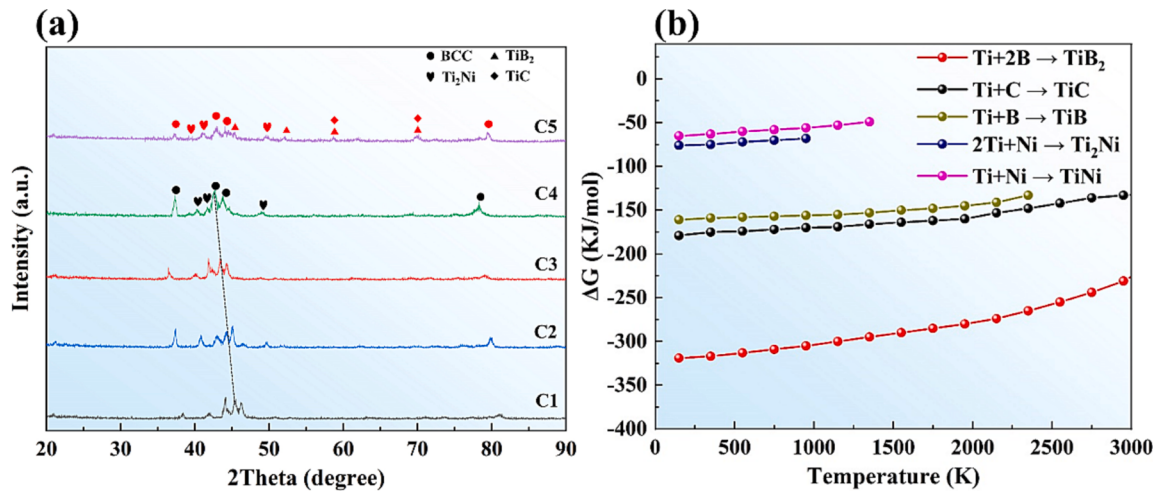


Fig. 7. Phase analysis of the C1–5: (a) the XRD patterns; (b) temperature dependent curve of Gibbs free energy (ΔG) in phase synthesis.

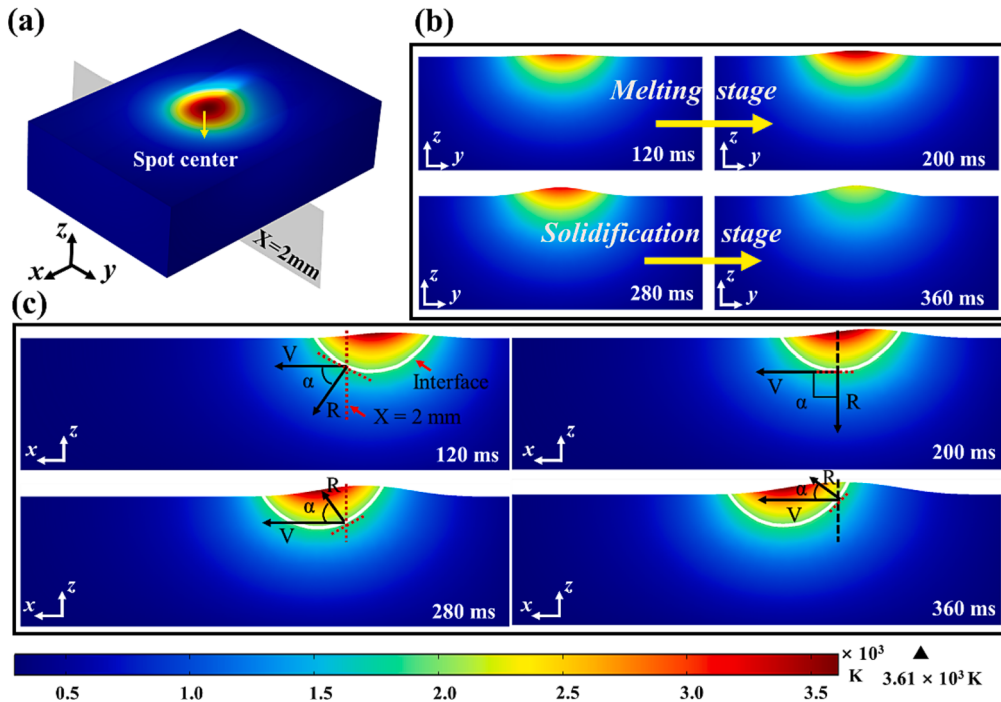


Fig. 8. (a) Simulated temperature distribution at 200 ms; (b) molten pool development history of C3 coating at $X = 2$ mm section; (c) temperature distribution diagram of xz cross-section at different time.

where T_L denotes the temperature of the liquid, T_0 denotes the initial temperature, K denotes the thermal conductivity and Q denotes the heat input. The α is the angle between the solidification interface and the scanning direction, as shown in Fig. 8(c). During the 120–200 ms, the reference cross section ($X = 2$ mm) is in the melting stage. As further LC progresses, the R gradually increases due to further reduces for α at 280 ms–360 ms.

Aiming to better understand the solidification behavior of the molten pool, as shown in Fig. 9, the values of G , R , G/R and G^*R are obtained at different times during the solidification stage (280 ms–360 ms) mentioned in Fig. 8. The G value at the front end of the solidification pool was greater than that at the back end (Fig. 9(a)), which was attributed to the influence of the pecklet characteristic length (L_p) and the convection velocity. According to the result of the velocity field, the L_p and convection velocity of the back end of the molten pool were larger.

The greater the L_p and convection velocity were, the more uniform the temperature distribution of the molten pool was, and the smaller the temperature gradient was. According to Eq. (10) and the morphology of molten pool, the α at the interface between the layer and the substrate was the maximum, where the R value was the lowest. As the position moved to the top of the molten pool, the α value was 1 approximately. Accordingly, the maximum value of R at the top of the molten pool is 9.79×10^{-3} m/s at 360 ms, which was approximately equal to V (10 mm/s), as shown in Fig. 9(b).

It was worth mentioning that morphological parameters (G/R) determined the type of dendrite, and cooling rate ($G \times R$) indicated the size of the dendrite. Specifically, the crystal type gradually changed from planar to cellular crystals, columnar, and equiaxed crystals as the G/R decreased according to the theory of rapid solidification of metals. In terms of the dendrite size, the $G \times R$ affected the constitutional undercooling (ΔT_c), thereby affecting the size of dendrite. The greater

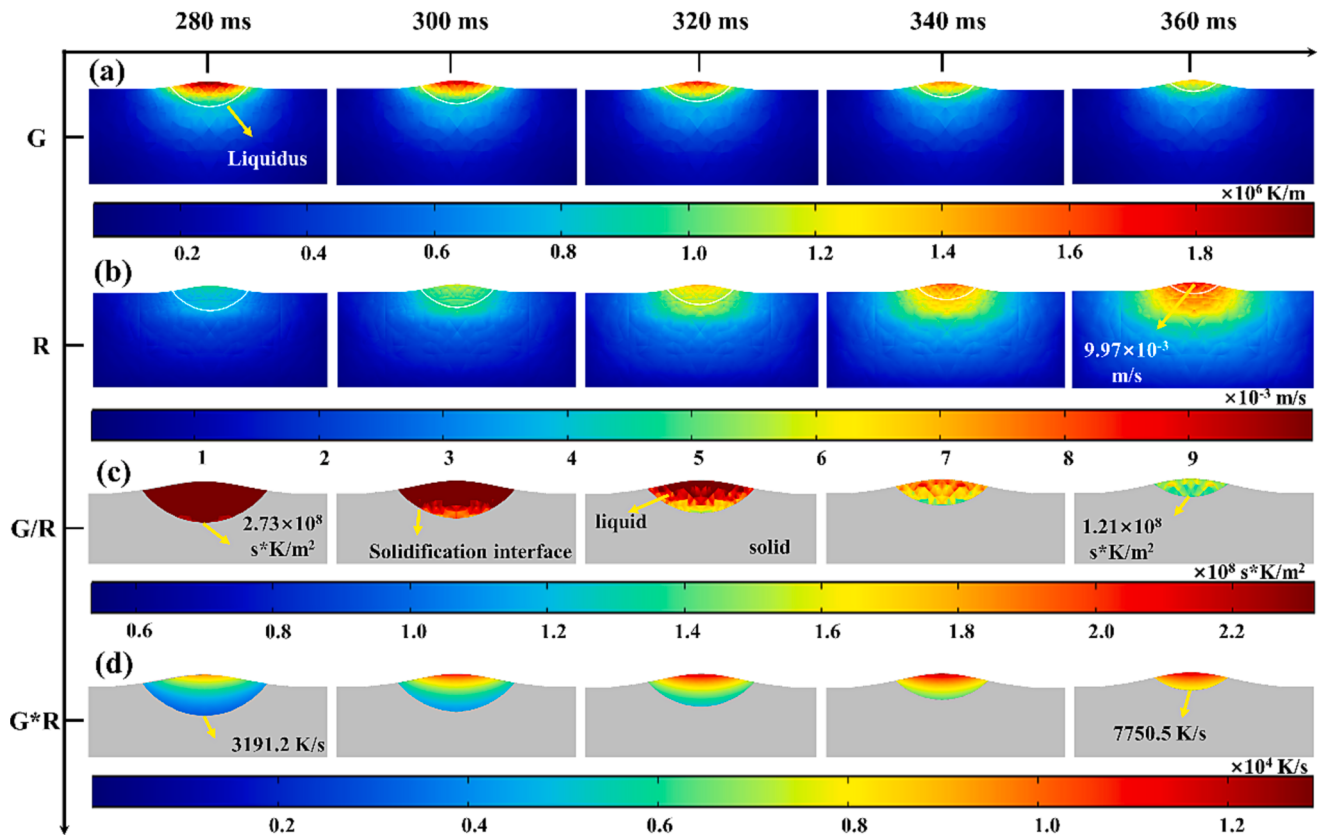


Fig. 9. Calculated solidification parameters of C3 coating at different times in molten pool ($X = 2 \text{ mm}$ section): (a) temperature gradient, G; (b) solidification rate, R; (c) morphological parameters, G / R ; (d) cooling rate, $G * R$.

the $G \times R$ was, the longer the time lag in crystalline nucleation of the material was, resulting in the finer the crystal was. Noticeably, the simulated G / R values underwent significant change as solidification proceeded. The G / R at the solidification interface gradually decreased from $2.73 \times 10^8 \text{ s}^* \text{K/m}^2$ at 280 ms to $1.21 \times 10^8 \text{ s}^* \text{K/m}^2$ at 360 ms, as shown in Fig. 9(c). Therefore, the crystal type gradually changes from planar crystals found at the bottom to cellular, columnar, and equiaxed crystals located at the top. In addition, the $G * R$ at the solidification interface gradually increased from 3191.2 K/s at 280 ms to 7750.5 K/s at 360 ms, as shown in Fig. 9(d), indicating that the dendrite size decreased from the bottom of the coating to the top of that.

To evaluate the reliability of the above simulation analysis, Fig. 10 displays the microstructure of the C3 coatings in different regions. Overall, the type of dendrite was different in the top, middle and bottom

of the coatings. Specifically, the bottom was mainly composed of planar and cellular crystals, while there were mainly columnar and equiaxed crystals in the middle of the coatings. At the top of the coatings, the grain structure was in the form of finer equiaxed crystal. Additionally, the grain size continuously decreased from bottom to top of coating. This was highly consistent with the evolution trend of solidification microstructure analyzed through simulation.

It is necessary to mention that the columnar crystal to equiaxed crystal transformation behavior (CET) appeared in the middle of C3 because of the low G/R value, as shown in Fig. 10(a2). The formation of equiaxed crystals was attributed to the fact that the high ΔT_c at the top of the coating met the undercooling required for heterogeneous nucleation (ΔT_n). The ΔT_n could be expressed as [53]:

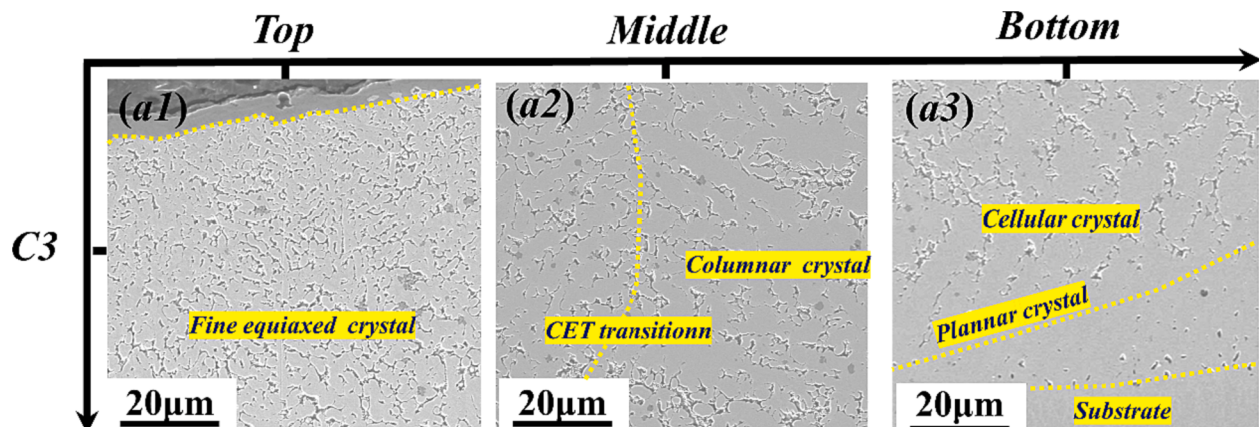


Fig. 10. The microstructure of C3 coating.

$$\Delta T_n = T_l - T_n \quad (11)$$

where T_l represents the liquidus temperature, and T_n refers to the nucleation temperature. The solidification began at the interface between the bottom of the molten pool and the substrate owing to the temperature difference. At the initial stage of solidification, dendrites only crystallized in a plane because of the narrow constitutional undercooled region. Therefore, the dendrites at the bottom of the coating mainly existed in the form of planar or cellular crystals. With the continuous expansion of constitutional undercooled region, the cellular crystals were replaced by coarse columnar crystals. It could be found that the secondary dendrite arms (SDAs) appeared at the top of the coating. The SDAs provided the probability of nucleation location for the formation of equiaxed crystals. At the same time, the high L_{ed} provided enough energy for that the ΔT_c was greater than ΔT_n , thus, promoting the occurrence of CET behavior.

Fig. 11 displays the microstructure of the C1, C2 and C4 coatings in different regions. The process route of coatings preparation significantly influenced the solidification parameters (g and r). It was well known that the Q in the molten pool increased with the increase of the L_{ed} . Since the L_{ed} of C1 and C2 coatings was low, the G/R values were relatively high. However, the formation of equiaxed grains required very low G/R, which indicated that there were no opportunity for the evolution of these grains in C1 and C2. As mentioned above, the SDAs was generated with approaching the top of the coating. The number of SDAs increased as L_{ed} increased, as shown in Fig. 10 (a1) and Fig. 11 (a1, b1, c1). It was due to the reduction in the solidification rate at the top of the layer so that the primary dendrite arms (PDAs) kept more opportunity to grow and nucleation. Additionally, the interdendritic metal liquid was insufficient to compensate and formed a cavity because of the gas in the molten pool, promoting the microporosity. It was one of the important

reasons why C1 and C2 kept high crack sensitivity. Interestingly, an increase of the L_{ed} to 73.33 $J\cdot mm^{-2}$ eliminate the microporosity and significantly refine the microstructure of C3 owing to the CET behavior. In summary, the appropriately increase of L_{ed} was conducive to the refinement of the grain. The quality and properties of the coating were improved thanks to the strengthening effect of fine grains [54].

Fig. 11 (d1-3) displays the microstructure of the C4 coating. Nevertheless, the excessive L_{ed} (80.0 $J\cdot mm^{-2}$) resulted in obvious solidification cracks in the coating. The above phenomenon could be explained as follows. Stress was the main factor that causes cracks in the coating [55]. The cooling time of the molten pool was prolonged as the heat input increased, which led to excessive substrate deformation. The stress on the coating increased under the constraint of the substrate. Additionally, the thermal stress in the form of tensile stress perpendicular to the fusion line also increased with the continuous increase in temperature gradient. Therefore, the cracks initiated from the bonding zone because of the stress exceeding the yield limit of the coating under the superposition of two types of stresses. It was worth noting that the microstructure of the C4 coating was still further refined. Undoubtedly, the uneven distribution of grains along grain boundaries and dislocation of dendrites weakened the grain refinement effect owing to the strong Marangoni convection effect in the molten pool.

Fig. 12 displays the microstructure of LaB₆/FeCoNiCrTi coating. It could be observed that the LaB₆ significantly influenced the microstructure of HEA coating. The dendritic type was mainly composed of coarse columnar crystals in the bottom of coating. A large amount of granular phase and rod-like phase appeared in the coating as the position moved upwards. Numerous studies [56,57] shown that Ti element had a strong affinity with C element and B element, which made it easy to generate TiB₂ (rod-like phase), TiC (dendrites phase) and TiB₂/TiC (flower-like phase). To further determine the phase types of rod-like,

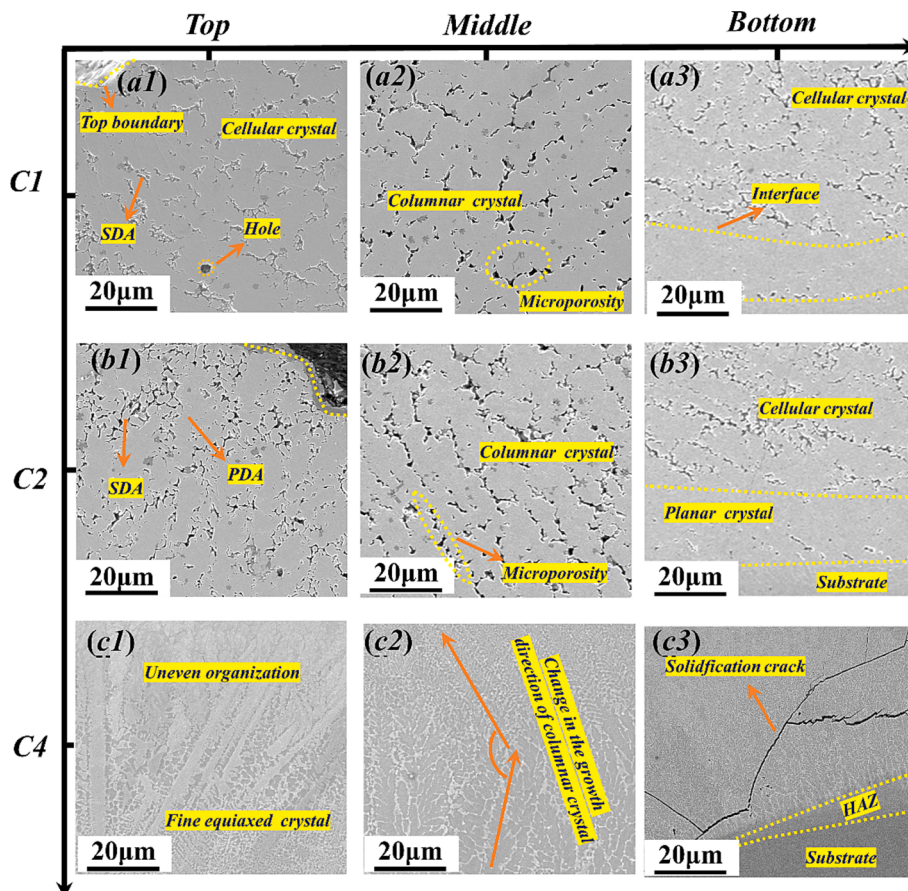


Fig. 11. The microstructure of C1, C2 and C4 coatings: (a1-3) C1; (b1-3) C2; (c1-3) C4.

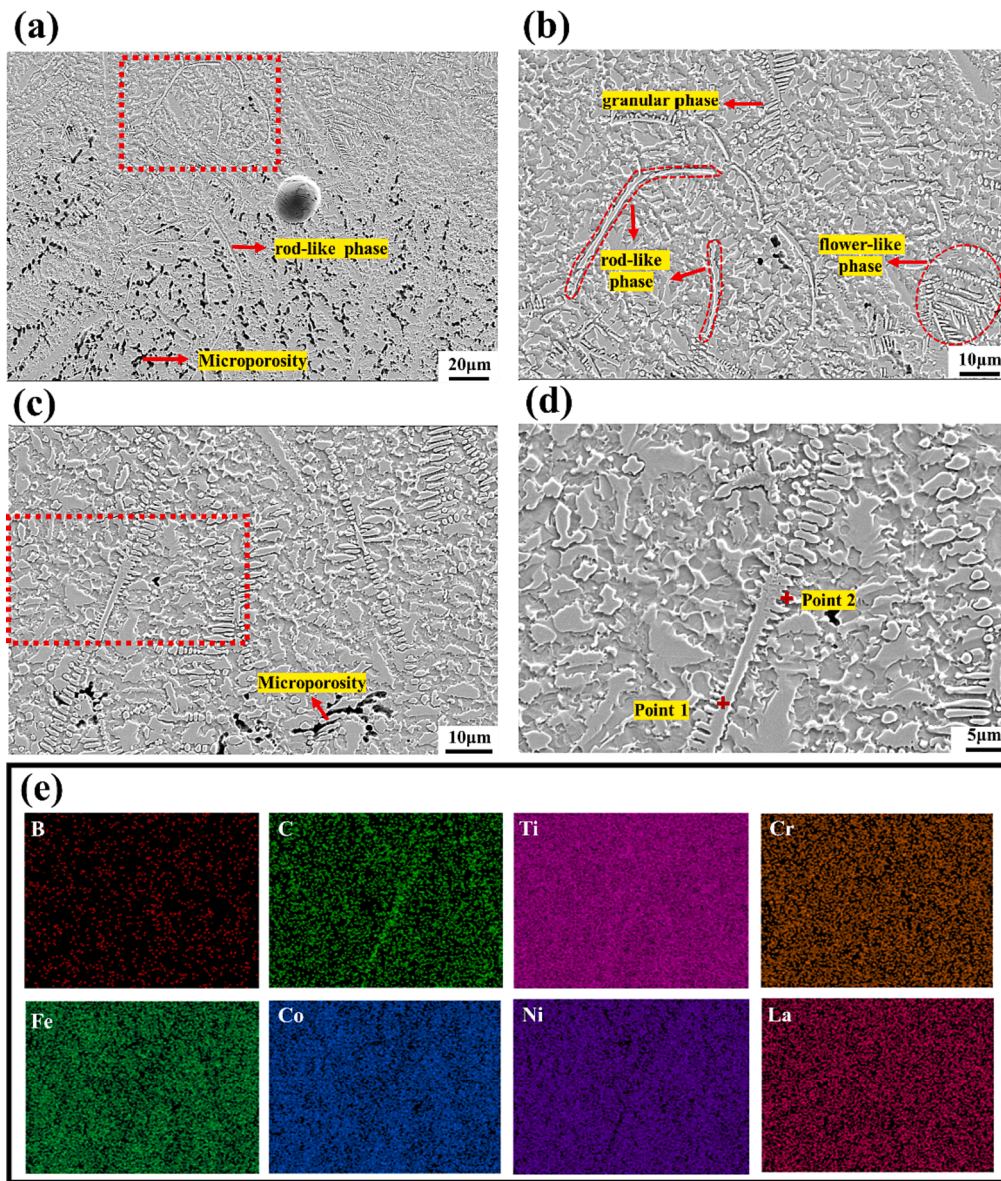


Fig. 12. Microstructure and EDS mapping of C5 coatings: (a) the bottom; (b) partial enlarged view of a; (c) the top; (d) partial enlarged view of c; (e) EDS mapping of d.

dendrites and flower-like phases, EDS mapping was used for element analysis of partial areas, as shown in Fig. 12(e). It could be found that the dendrites of the flower-like phases were rich in C and Ti elements. However, the B element cannot be identified because of the low sensitivity to EDS. Hence, the Point 1 and Point 2 were selected for the EDS analysis. The results show that the rod-like is mainly composed of Ti and B elements, while the dendrite phase is mainly composed of Ti and C elements, as shown in Table 3. More specifically, the atom ratio of Ti and B elements in point 1 was 1:1.82, which could be considered as TiB₂ (Point 1) owing to the spot analysis error of EDS. Furthermore, the atom ratio of Ti and C elements in point 2 was approximately 1:1, which was

considered as the TiC.

Noticeably, the flower-like phase was composed of rod-like phase and dendrite phase, namely TiB₂/TiC eutectic structure. During the LC process, Ti6Al4V and LaB₆/FeCoNiCrTi powder were melted into the molten pool, and a large amount of Ti element reacted with B and C element to generate TiB₂ and TiC. Compared with the TiC, the TiB₂ precipitated preferentially owing to its low ΔG value in Section 3.2. It can be observed that long-rod shaped TiB₂ is distributed at the front end of coarse columnar crystals, as shown in Fig. 12(a). The appearance of TiB₂ hindered the further growth of columnar crystals, which eliminated the microporosities in the coating. Noticeably, the TiB₂ enriched a large number of Ti and C atoms, and TiC considered TiB₂ as the most effective heterogeneous nucleation core. As the distance from the coating surface decreased, the TiC grew around TiB₂ to form a composite structure (TiB₂/TiC eutectic structure) since the nucleation conditions of TiC met the requirements. TiC and TiB₂ grew and constrain each other, which could generate a fine grain strengthening effect.

Table 3
EDS analysis results of Point 1 and 2 in Fig. 12(d).

Region	Elements (At %)							
	Fe	Co	Ni	Cr	Ti	La	B	C
1	6.3	9.6	8.7	5.9	22.6	0.0	41.1	5.8
2	7.7	8.9	7.3	6.4	34.9	0.1	5.0	29.7

3.4. Microhardness

Fig. 13(a) shows the microhardness distribution of the C1-C5 coatings from the top surface to the substrate (Ti6Al4V). Conspicuously, every coating had a consistent hardness distribution rule. The microhardness of the coating area, HAZ and substrate area were significantly different. More specifically, the average microhardness of C1 coating and C5 coating were 1.38 times and 1.59 times that of Ti6Al4V, respectively, as shown in the Fig. 13(b). Hence, the preparation of HEA coating was a reliable way to improve the microhardness of the substrate. Besides, the microhardness of the C2-4 coatings increased compared with that of C0 coating, indicating that L_{ed} played a critical role of microhardness. The increase of L_{ed} resulted in a decrease in the grain size of the coatings according to the conclusions discussed above. According to the Hall-Petch [58] effect, the strength of the material was inversely proportional to the grain size. Notably, the strength of the material came from the activation of dislocation sources within the grain caused by external forces. The dislocation forest was hindered by grain boundary, causing the stress strengthening of the material [59]. As a result, a decrease in grain size increased the number of grain boundaries and the movement of dislocations. Ultimately, the plastic deformation of the material was restrained. Simultaneously, it could be observed that the hardness distribution curve of C4 coating was not smooth enough. It was due to that the microhardness measurement point was close to the defects, which weakened the dislocation mechanism and caused the decrease of microhardness.

For another, the average microhardness of C5 coating was 593 HV_{0.2}, which was much higher than C1-C4 coatings. It was attributed to the in-situ generation of TiB₂ and TiC reinforcing phases in the coating, which significantly improved the microhardness of HEA coatings. As the typical ceramic phase particle, the TiB₂ and TiC played a dispersed strengthening and supporting role [31]. In brief, the regulation of laser process parameters and addition of rare earth phase particles could improve the mechanical properties of coatings.

3.5. Corrosion behavior

Fig. 14 displays the potentiodynamic polarization curves (PDP) of the substrate (Ti6Al4V) and C1-C5 coatings in 3.5 wt% NaCl solution. It could be seen that the doping of LaB₆ significantly expanded the passivation range of the coating, indicating an improvement in the stability of the passivation film. However, the influence of L_{ed} is relatively small on stability of the passivation film. According to the tafel law [60], there existed a linear function of E (electrode potential) and

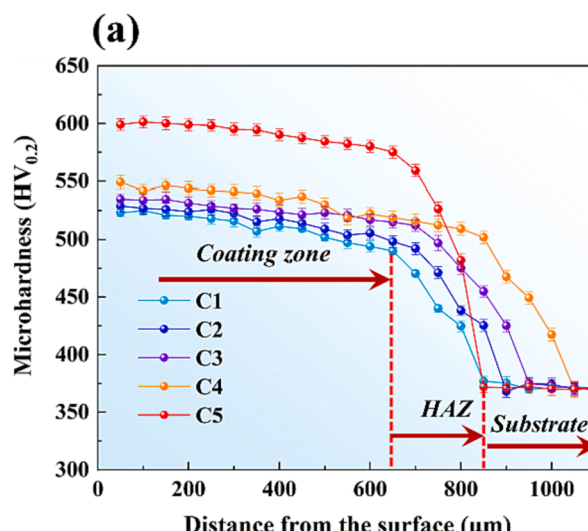


Fig. 13. The microhardness of coatings of C1-C5: (a) microhardness distribution curve; (b) the average microhardness.

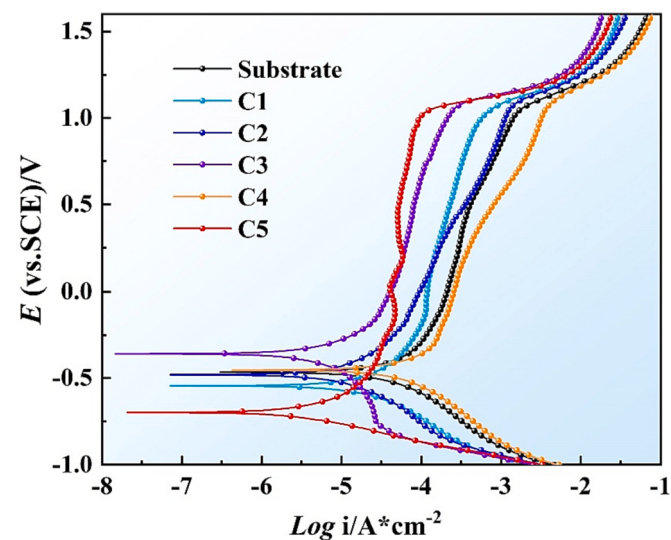
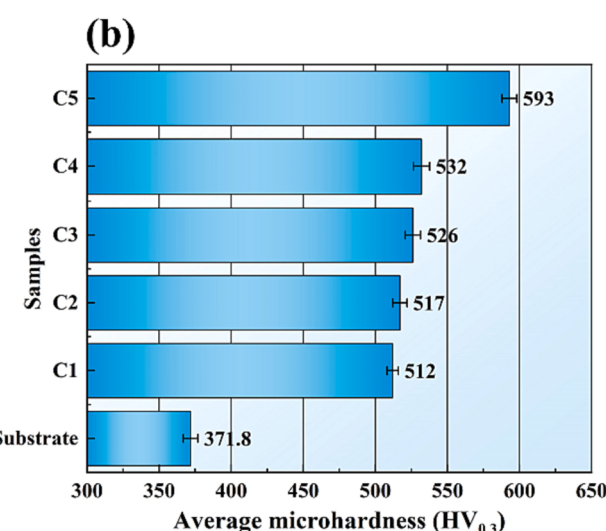


Fig. 14. The potentiodynamic polarization curves of Ti6Al4V and C1-C5 coatings.

$\log [i]$ (current density) in Tafel area of PDP curve. The E_{corr} (corrosion potential) and I_{corr} (corrosion current density), which were obtained through extrapolation, are listed in Table 4. It was worth mentioning that I_{corr} and E_{corr} were corrosion kinetics and thermodynamic behaviors, respectively. The corrosion rate of material was positively correlated with I_{corr} , indicating that the faster the corrosion rate when the I_{corr} was higher, and the poorer the corrosion resistance [61]. The I_{corr} of Ti6Al4V, C1, C2, C3, C4 and C5 were $3.201 \times 10^{-5} \text{ A}\cdot\text{cm}^{-2}$, $1.605 \times 10^{-5} \text{ A}\cdot\text{cm}^{-2}$, $8.802 \times 10^{-6} \text{ A}\cdot\text{cm}^{-2}$, $4.796 \times 10^{-6} \text{ A}\cdot\text{cm}^{-2}$, $5.312 \times 10^{-5} \text{ A}\cdot\text{cm}^{-2}$ and $2.400 \times 10^{-6} \text{ A}\cdot\text{cm}^{-2}$. The data showed very clearly that the

Table 4
Electrochemical parameters of Ti6Al4V and C1-C5 coatings.

Sample	E_{corr} (V _{vs.SCE})	I_{corr} (A·cm ⁻²)
Substrate (Ti6Al4V)	-0.465	3.201×10^{-5}
C1	-0.544	1.605×10^{-5}
C2	-0.480	8.802×10^{-6}
C3	-0.341	4.796×10^{-6}
C4	-0.454	5.312×10^{-5}
C5	-0.698	2.400×10^{-6}



corrosion resistance in ascending order were: C4 < Ti6Al4V < C1 < C2 < C3 < C5. On the one hand, the E_{corr} of HEA coating reached its peak (-0.341 V vs. SCE) and the value of I_{corr} was lowest at the energy density of 73.33 J/mm^{-2} . When the laser energy density was 80 J/mm^{-2} , its corrosion resistance was even worse than that of the substrate owing to defects. Hence, the HEA coating increased the corrosion resistance of Ti6Al4V at a certain energy density. On the other hand, the I_{corr} of LaB₆/HEA composite coating (C5) was twice that of HEA coating (C3) under the same process parameters, indicating that the doping of LaB₆ could significantly improve the corrosion resistance. This phenomenon could be attributed to the fact that the corrosion resistance of the coating was closely related to its microstructure. The corrosion resistance behavior of the coatings was significantly affected by the dendrite structure. The finer grain could provided more active sites for the nucleation and growth of the passive film [62]. As a result, the fine grain strengthening effect mentioned in Section 3.3 was achieved through the optimization of L_{ed} and the doping of LaB₆, resulting in excellent corrosion resistance of the coatings.

To investigate the actual corrosion of the coatings in the 3.5 wt% NaCl solution, Fig. 15 displays the corrosion morphology after PDP testing. It could be observed that white circular pits were randomly distributed on the coatings surface, namely corrosion pits. Obviously, the number of pitting pits in C1, C2 and C4 coatings were significantly greater than that in C3 and C5 coatings. In addition, the size (depth and width) of corrosion pits was measured by Laser Confocal Microscope. Among them, the maximum pitting widths of C1-C4 coatings were 91.10 μm , 81.00 μm , 22.40 μm and 24.60 μm , respectively. The maximum depths were 42.86 μm , 35.63 μm , 9.58 μm and 21.81 μm , respectively. It could be inferred that L_{ed} significantly affected the probability of pitting corrosion occurring. During the solidification process of the molten pool, an appropriate L_{ed} was beneficial for the removal of inclusions, thereby reducing the number of active particles on the coating surface. The consistent surface potential greatly reduced the number of micro-corrosive batteries and the tendency for pitting corrosion. However, the cracks had a negative impact on the corrosion resistance of the coating. Narrow cracks could limit the diffusion of oxygen, resulting in a difference in oxygen concentration inside and outside the coating cracks, which promoted the pitting corrosion occurrence. Accordingly, the C4 coating with more cracks exhibitd the poorer corrosion resistance.

It was worth mentioning that corrosion pits were also closely related to the coating microstructure. Corrosion pits were formed by the combined action of local anode position in the electric field and the concentration of Cl⁻ ions. According to the T. Okada's theory of perturbation-induced pitting corrosion [63], the probability of pitting nucleation could be evaluated by comparing the spacing of anodic site (l) and the critical wavelength of the perturbations (λ_c). Specifically, the probability of pitting corrosion was high when $l > \lambda_c$. Consequently, a finer microstructure meant a smaller l , which led to a lower probability of pitting corrosion or a smaller size of pitting. Surprisingly, the corrosion morphology of LaB₆/FeCoNiCrTi composite coating exhibits a smooth plane with only a few small corrosion pits, as shown in Fig. 15(e). It could be inferred that the doping of LaB₆ resulted in grain refinement, which reduced the l and made the most area of the coating meet the $l < \lambda_c$. The results were consistent with the PDP analysis. Fig. 15(f) shows the elements distribution in the corrosion morphology of C2 coating. It could be observed that there was significant differences in the distribution of elements inside and outside the corrosion pits. Ti element enrichment in corrosion pits indicated that Ti element played a key role in improving the corrosion resistance of coatings.

3.6. Passivation film analysis

The properties of passivation film were an important indicator for evaluating the difficulty level of corrosion. As a result, the electrochemical impedance spectroscopy (EIS) was used for analyzing the

passivation film. Fig. 16(a) displays the Nyquist plots of the samples (substrate and C1-5 coatings) in the the 3.5 wt% NaCl solution. It could be clearly observed that coatings exhibited different capacitive arcs under different process routes, indicating significant differences in charge transfer systems [64]. Noticeably, the diameter of the capacitive arc was directly proportional to the charge transfer resistance, which meant that the larger the diameter was, the better the corrosion resistance was. The results showed that the diameter of the capacitive arc was arranged in ascending order: C4 < Ti6Al4V < C1 < C2 < C3 < C5, which was consistent with the conclusion obtained from the PDP curve.

In terms of metal coatings, the electrochemical corrosion process covered corrosion solution/passivation film/electrode/metal. Hence, a equivalent circuit model with two-time constants (R (Q (R (QR)))) was used for EIS fitting to further analyze the passivation behavior in this work, as shown in Fig. 16(b). Simultaneously, Fig. 16(c) displays the Bode plots (impedance ($|Z|$) and phase angles) of the samples. Bode impedance in high-frequency (10^4 - 10^5) region represented the the resistance of 3.5 wt% NaCl solution, while the low-frequency region represented the charge transfer resistance. It could be preliminarily determined that the doping of LaB₆ and the regulation of L_{ed} can significantly affected the charge transfer resistance of the coating. In the phase angle curve, the negative phase angle reached its peak near the intermediate frequency range (10^{-1} - 10^1 Hz), exhibiting a typical capacitive impedance characteristics. Furthermore, the corrosion resistance of the passivation film was positively correlated with the negative phase angle peak value. The peak value of C3 coating was approximately 65°, indicating that a dense passivation film was formed on the surface of the HEA coating. The dense passivation film effectively blocked the corrosive solution and delayed the breakdown of the coating under external voltage [65].

The EIS fitting parameters are listed in the Table. 5. Among them, R_s and R_f were the resistance of 3.5 wt% NaCl solution and the passive film resistance on the metal coating surface, respectively. Q_f represented the capacitance between the passivation film and the corrosion solution. R_{ct} and Q_{dl} represented charge transfer resistance and capacitance between the samples and the solution owing to the passive film was damaged, respectively. Normally, the Chi-squared (χ^2) was used to evaluate the reliability of EIS fitting results. The χ^2 value of all samples was between 10^{-3} and 10^{-4} , which verified the reliability of EIS fitting results. It was worth pointing out that the polarization resistance of the sample could be expressed as [66,67]: $R = R_s + R_f + R_{ct}$. It could be found that the value of R_{ct} was much greater than R_s and R_f , indicating a positive correlation between the corrosion resistance of the sample and R_{ct} . More specifically, the R_{ct} values of Ti6Al4V, C1, C2, C3, C4 and C5 coatings were $4.21 \times 10^3 \Omega^* \text{cm}^2$, $7.037 \times 10^3 \Omega^* \text{cm}^2$, $1.164 \times 10^4 \Omega^* \text{cm}^2$, $1.493 \times 10^4 \Omega^* \text{cm}^2$, $1.893 \times 10^3 \Omega^* \text{cm}^2$ and $4.348 \times 10^4 \Omega^* \text{cm}^2$, respectively. The corrosion resistance of C1, C2, C3, and C5 was greater than that of the substrate, which was consistent with the results of analyzing the Nyquist curve. Unfortunately, the abnormal phenomenon observed in the C4 coating was attributed to a large number of macroscopic cracks, which accelerated the invasion of ions into the material and thereby reduced its corrosion resistance.

Analyzing the formation and dissolution process of passivation film was a crucial step in evaluating the corrosion resistance of coatings. Currently, analyzing the semiconductor properties and the charge carrier density of passivation films by using the Mott-Schottky method [68,69] was a mainstream method. It was particularly pointed out that the space charge capacitance of the passivation film was related to the applied potential, which could be expressed as:

$$\frac{1}{C^2} = \pm \frac{2}{A^2 \epsilon \epsilon_0 e N_x} (E - E_{fb} - \frac{kT}{e}) \quad (12)$$

where C represents the interfacial capacitance, A is the surface area of the specimen (1 cm^2), e is the charge of the electron ($1.602 \times 10^{-19} \text{ C}$), E_{fb} is the flat band potential, ϵ and ϵ_0 are the permittivity of the passive

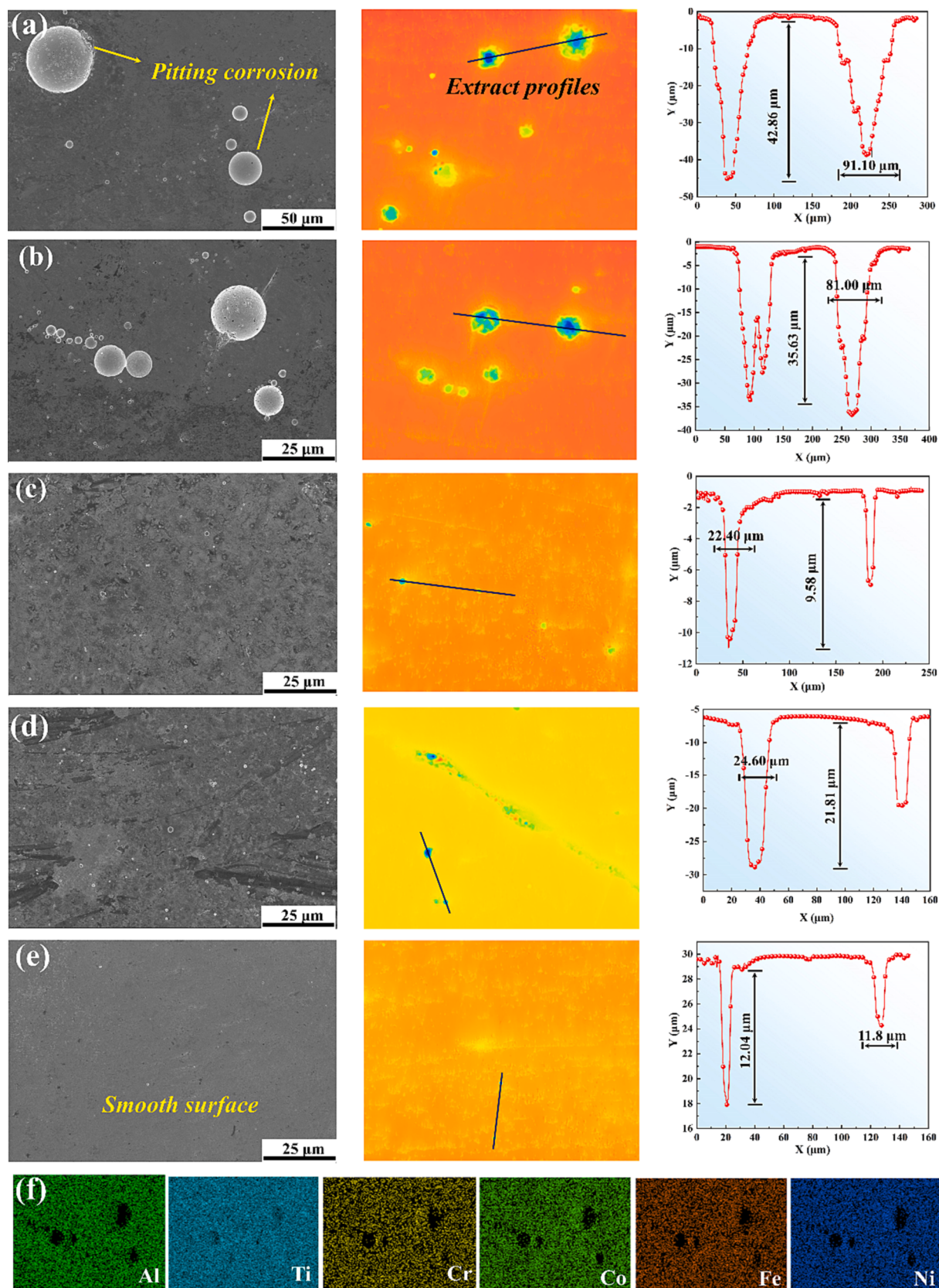


Fig. 15. Corrosion morphology dominated by pitting pits: (a) C1; (b) C2; (c) C3; (d) C4; (e) C5; (f) EDS mapping results of C2.

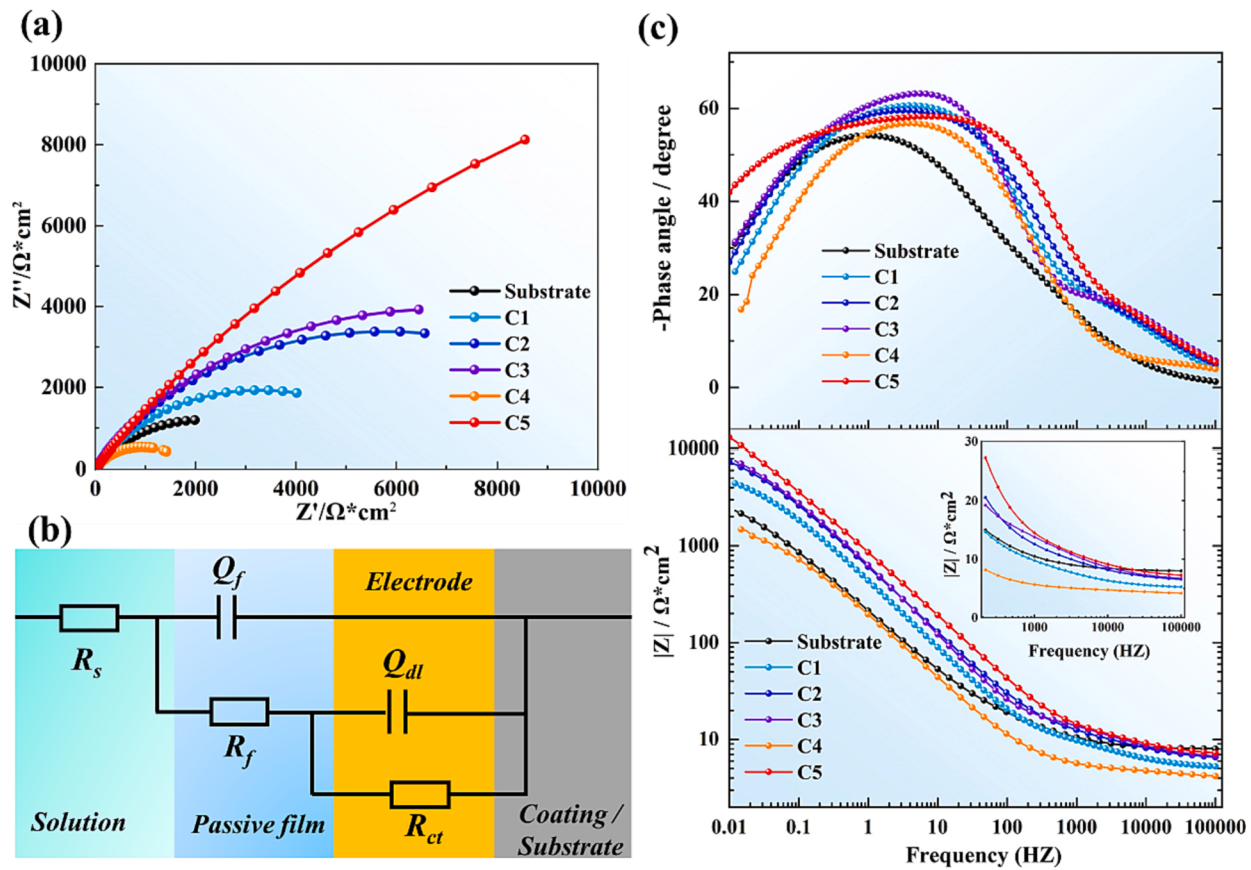


Fig. 16. EIS of Ti6Al4V and C1–C5 coatings: (a) Nyquist plots; (b) Bode plots; (c) equivalent circuit of EIS.

Table 5
EIS fitting parameters of Ti6Al4V and C1–C5 coatings.

	Substrate	C1	C2	C3	C4	C5
$R_s (\Omega * \text{cm}^2)$	7.893	4.967	6.128	6.158	3.829	6.697
$Q_f Y_0 (\text{F} \cdot \text{cm}^{-2})$	9.579×10^{-4}	4.697×10^{-4}	2.929×10^{-4}	3.480×10^{-4}	6.932×10^{-4}	3.193×10^{-4}
$Q \cdot n_1$	0.6381	0.6266	0.6313	0.6053	0.5866	0.6106
$R_f (\Omega * \text{cm}^2)$	31.45	10.87	10.59	15.91	1.51	14.89
$Q_{dl} Y_0 (\text{F} \cdot \text{cm}^{-2})$	4.485×10^{-4}	1.672×10^{-4}	1.033×10^{-4}	1.681×10^{-4}	7.392×10^{-4}	6.909×10^{-5}
$Q \cdot n_2$	0.7003	0.7674	0.8321	0.8999	0.7410	0.8565
$R_{ct} (\Omega * \text{cm}^2)$	4.21×10^3	7.037×10^3	1.164×10^4	1.493×10^4	1.893×10^3	4.348×10^4
$\chi^2 (\times 10^{-3})$	1.353	2.811	0.9119	1.540	1.886	2.191

film at room temperature (15.6) and vacuum permittivity ($8.854 \times 10^{-14} \text{ F/cm}$), respectively. k is the Boltzmann constant ($1.38 \times 10^{-23} \text{ J K}^{-1}$), T is the absolute temperature, N_x denotes the charge carrier density, including N_A (acceptors) and N_D (donors). The Plus-minus sign represents the semiconductor type, that is, the positive sign is n-type semiconductor, the negative sign is P-type semiconductor. According to Eq. (12), N_x could be calculated as:

$$N = \frac{2}{A^2 \lambda \epsilon e_0} \quad (13)$$

where λ represents the slope of the straight line segment in the Mott Schottky curve, as shown in Fig. 17(a). The slopes of the curves were all positive, indicating that the passivation films were the n-type semiconductor on the surface of the HEA coatings. In addition, the curves exhibited a partial nonlinear relationship, which was caused by the non-uniformity and adsorption effect of the passivation film [70].

Based on the slope of the yellow solid line, the N_D of the passivation films were calculated (Fig. 17(b)). The N_D of Ti6Al4V and C1–C5 coatings are $3.084 \times 10^{22} \text{ cm}^{-2}$, $1.659 \times 10^{22} \text{ cm}^{-2}$, $1.889 \times 10^{22} \text{ cm}^{-2}$,

$1.556 \times 10^{22} \text{ cm}^{-2}$, $7.536 \times 10^{22} \text{ cm}^{-2}$ and $1.053 \times 10^{22} \text{ cm}^{-2}$, respectively. As a matter of fact, the most common carriers existed in the form of doped oxygen vacancies or cation gaps in the n-type semiconductors [71]. The property of n-type semiconductors was described as that the electrons attracted by oxygen vacancies were the donors in the barrier layer between the passivation film and solution. The Cl^{-1} in the NaCl solution accelerated the accumulation of oxygen vacancies in the barrier layer, which was the main reason for the breakdown of the passivation film [72]. Hence, the increase of N_D caused gaps between the passivation film and the coating, which delayed the formation of the passivation film and promoted the pitting defects. The data shows very clearly that the N_D of C4 coating is higher than that of the other samples. Specifically, the defects inherent in the C4 coating allowed the corrosion solution to penetrate, resulting in a severe corrosion reaction and rapid transfer of electrons. Additionally, the N_D of C5 and C3 coatings was only one-third of that of the substrate. The passive film kept better barrier property to electron transfer and stability with lower N_D , resulting in more excellent corrosion resistance of coatings.

The thickness of the passivation film is one of the important pa-

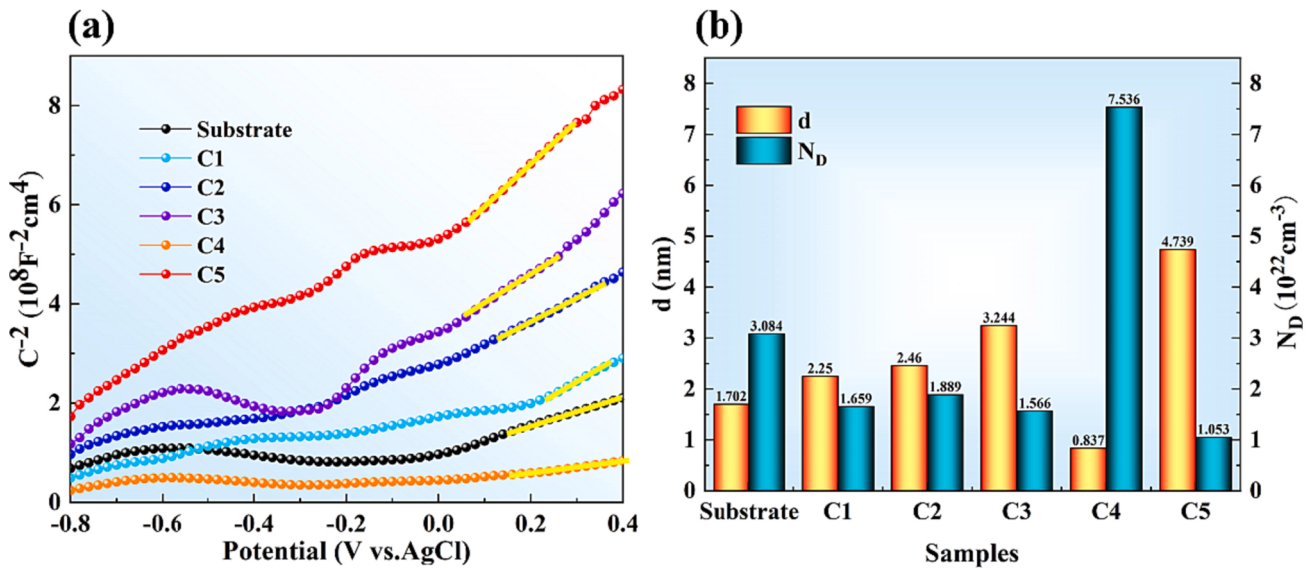


Fig. 17. Passivation film analysis of Substrate and C1–C5 coatings: (a) Mott-Schottky plots; (b) donors densities (N_D) and thickness (d) of the passive films.

parameters for evaluating the corrosion resistance of coatings. The thicker the passivation film is, the stronger its ability to resist Cl⁻ ions is and higher corrosion resistance exhibit. The value of thickness (d) can be expressed as follows [73,74].

$$d = \frac{(\epsilon\epsilon_0)^n A}{g Q \rho_d^{(n-1)}} \quad (14)$$

$$g = 1 + 2.88(1 - n)^{2.375} \quad (15)$$

where Q denotes the possibility of a non-ideal capacitance (CPE, i.e. Q_{dl}), ρ_d is the resistivity ($\rho_d = 500 \text{ cm}^2$) and n is the surface inhomogeneity exponent. Based on EIS fitting data (Table 5), the thickness of the passivation film is calculated, as shown in Fig. 17(b). The d of Ti6Al4V

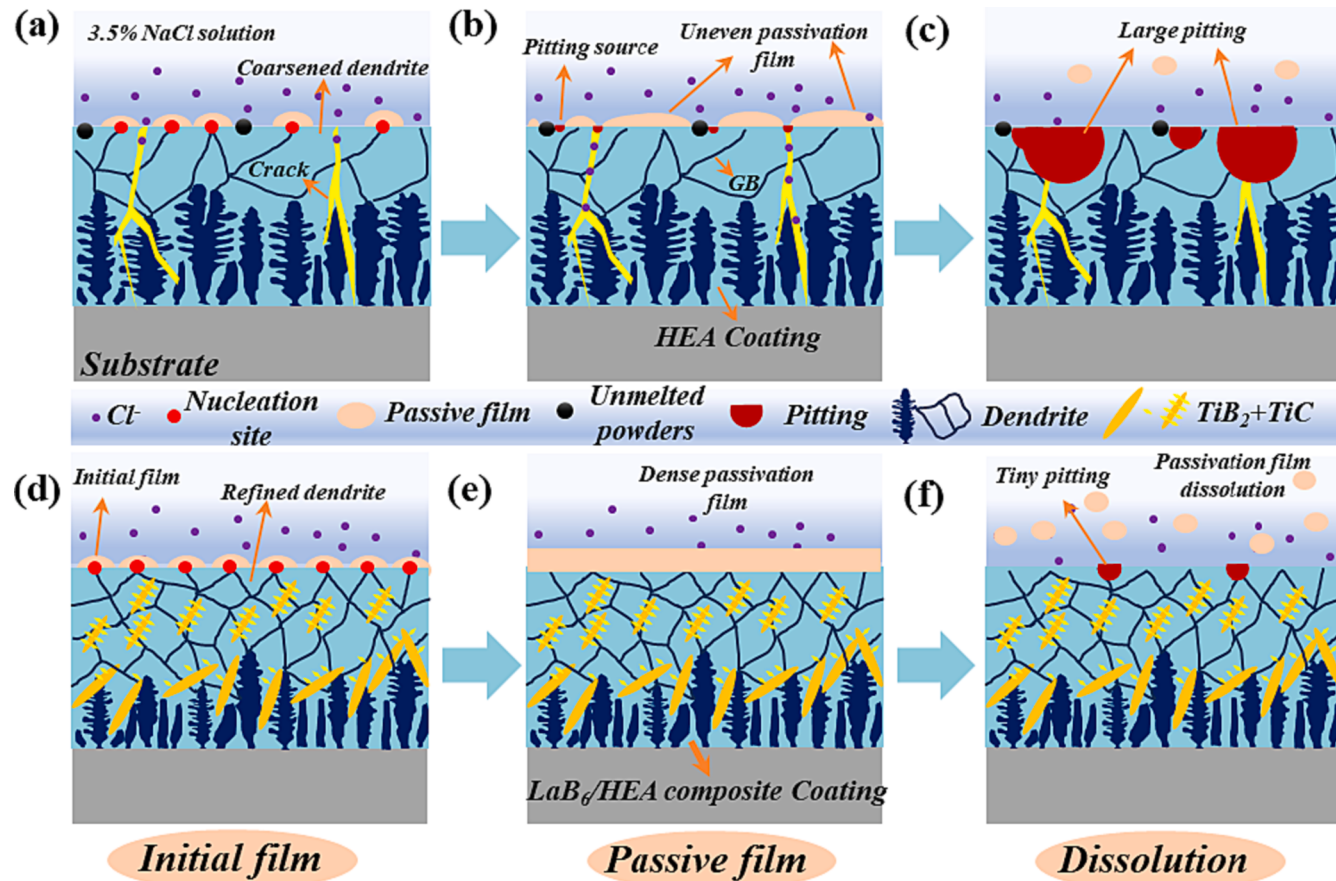


Fig. 18. The mechanism of passivation film nucleation, formation process and dissolution: (a–c) Coatings with poor forming quality; (d–f) LaB₆/HEA composite coating.

and C1-5 coatings were 1.702 nm, 2.250 nm, 2.460 nm, 3.244 nm, 0.837 nm and 4.739 nm. The pattern of d was consistent with N_D and R_{ctb} indicating a positive correlation between the formation rate of passivation film and d . The higher the repair rate of the passivation film was, the greater its thickness value was, and the better the corrosion resistance of the coatings was.

To more clearly identify the corrosion behavior of coatings in NaCl solution, the passivation mechanism of HEA and LaB₆/HEA composite coating are shown in Fig. 18. For the coatings with poor forming quality, the passivation film needed a longer spreading time over the surface due to coarse dendrites and unmelted powder, which led to uneven thickness of the passivation film, as shown in Fig. 18(a–c). In addition, cracks could exacerbate corrosion and promote the generation of pitting. Conversely, the refined dendrites provided more nucleation points, which were conducive to the rapid development of the passivation film over the coating surface. As shown in Fig. 18(d–f), the initial films connected with each other in a short time to form a complete and dense passivation film, which significantly improved the corrosion resistance of the coating. On the whole, the LaB₆ doping and regulation of L_{ed} played a positive role in the corrosion resistance of coatings.

4. Conclusions

In this paper, HEA coatings were fabricated on Ti6Al4V under different L_{ed} and doping-LaB₆ via laser cladding technology. Simultaneously, a series of characterization (XRD, SEM and EDS) and properties testing experiments were conducted to analyze the single-track morphology, microstructure, microhardness and corrosion resistance of the coatings. Based on the analysis results, the following conclusions are obtained.

1. The optimization of L_{ed} and the doping - LaB₆ had a significant impact on the morphology and crack sensitivity of single-track. The coating with L_{ed} of 73.33 J/mm² and LaB₆/FeCoNiCrTi composite coating exhibited excellent forming quality.
2. Based on XRD, Gibbs free energy calculations, SEM, simulation and EDS analysis, the phase types of the coatings were independent of L_{ed} . The improvement of L_{ed} and the doping - LaB₆ made the coating microstructure more uniform and finer. Simultaneously, TiB₂ and TiC were generated in LaB₆/FeCoNiCrTi composite coating. Intriguingly, TiB₂ could be served as the most effective nucleation core for TiC to improve nucleation rate and refine TiC (TiB₂ – TiC composite structure).
3. The microhardness of HEA coatings were much higher than that of the substrate (Ti6Al4V). Among them, the average microhardness of C5 coating was improved to 593 HV_{0.2} which was much higher than C1-C4 owing to the dispersion strengthening effect of ceramic particles.
4. The larger the N_D value of the passivation film is, the faster its repair rate is and the larger thickness value of the passivation film is, resulting in improvement of corrosion resistance of coatings. The I_{corr} , N_D and d of C3 were 4.796×10^{-6} A·cm⁻², 1.556×10^{22} cm⁻² and 3.244 nm, respectively. The I_{corr} , N_D and d of C5 were 2.400×10^{-6} A·cm⁻², 1.053×10^{22} cm⁻² and 4.739 nm, respectively. Consequently, the regulation of L_{ed} and the doping-LaB₆ can significantly improve the corrosion resistance of coatings.

CRediT authorship contribution statement

Dadong Jie: Formal analysis, Investigation, Methodology. **Meiping Wu:** . **Rui He:** Validation, Writing – review & editing. **Chen Cui:** Conceptualization, Project administration, Supervision. **Yuling Gong:** Formal analysis. **Xiaojin Miao:** Funding acquisition, Project administration, Supervision.

Declaration of competing interest

The authors declare that they have no known competing financial interests or personal relationships that could have appeared to influence the work reported in this paper.

Data availability

Data will be made available on request.

Acknowledgements

This work was financially supported by Research on Quality Control of Laser Cladding Remanufacturing for Repairing Damaged Aeroengine Blades (No. 8091B032207).

References

- [1] I.V. Okulov, A.S. Volegov, H. Attar, et al., Composition optimization of low modulus and high-strength TiNb-based alloys for biomedical applications, *J. Mech. Behav. Biomed. Mater.* 65 (2017) 866–871.
- [2] L.L. Bai, J. Li, J.L. Chen, et al., Effect of the content of B4C on microstructural evolution and wear behaviors of the laser-clad coatings fabricated on Ti6Al4V, *Opt. Laser Technol.* 76 (2016) 33–45.
- [3] H.X. Zhang, H.J. Yu, C.Z. Chen, et al., Microstructure and dry sliding wear resistance of laser cladding Ti-Al-Si composite coating, *Surf. Rev. Lett.* 2 (2018) 1–10.
- [4] J.W. Pegues, S. Shao, N. Shamsaei, et al., Fatigue of additive manufactured Ti-6Al-4V, Part I: The effects of powder feedstock, manufacturing, and post-process conditions on the resulting microstructure and defects, *Int. J. Fatigue.* 132 (2020) 105358.
- [5] H. Gasan, E. Lokcu, A. Ozcan, et al., Effects of Al on the phase volume fractions and wear properties in the AlxCoCrFeMoNi high entropy alloy system, *Met. Mater. Int.* 26 (2020) 310–320.
- [6] J. Li, Y. Huang, X. Meng, et al., A review on high entropy alloys coatings: fabrication processes and property assessment, *Adv. Eng. Mater.* 21 (8) (2019) 1900343.
- [7] K. Jin, Z. Yang, P. Chen, et al., Modeling of solidification process during multi-track laser cladding with 3D cellular automata coupling gas-liquid interface tracking and solute suppression nucleation, *J. Mater. Process Tech.* 315 (2023) 117927.
- [8] M. Li, B. Han, L. Song, et al., Enhanced surface layers by laser cladding and ion sulfurization processing towards improved wear-resistance and self-lubrication performances, *Appl. Surf. Sci.* 503 (2020) 144226.
- [9] C. Liu, C. Li, Z. Zhang, et al., Modeling of thermal behavior and microstructure evolution during laser cladding of AlSi10Mg alloys, *Opt. Laser Technol.* 123 (2020) 105926.
- [10] Z.Q. Cui, Z. Qin, P. Dong, et al., Microstructure and corrosion properties of FeCoNiCrMn high entropy alloy coatings prepared by high speed laser cladding and ultrasonic surface mechanical rolling treatment, *Mater. Lett.* 59 (2020) 126769.
- [11] K.V. Thurston, B. Gludovatz, A. Hohenwarter, et al., Effect of temperature on the fatigue-crack growth behavior of the high-entropy alloy CrMnFeCoNi, *Intermetallics* 88 (2017) 65–72.
- [12] H. Wang, W. Zhang, Y. Peng, et al., Microstructures and wear resistance of FeCoCrNi-Mo high entropy alloy/diamond composite coatings by high speed laser cladding, *Coatings* 10 (3) (2020) 300.
- [13] S. Zhang, C.L. Wu, C.H. Zhang, et al., Laser surface alloying of FeCoCrAlNi high-entropy alloy on 304 stainless steel to enhance corrosion and cavitation erosion resistance, *Opt. Laser Technol.* 84 (2016) 23–31.
- [14] H. Liu, J. Liu, P. Chen, et al., Microstructure and high temperature wear behaviour of in-situ TiC reinforced AlCoCrFeNi-based high-entropy alloy composite coatings fabricated by laser cladding, *Opt. Laser Technol.* 118 (2019) 140–150.
- [15] R. Zhang, X.Y. Gu, H.T. Gong, et al., Effect of Nb content on microstructure and properties of FeCoNi2CrMnV0.5Nb high-entropy alloy coatings by laser cladding, *J. Mater. Res. Technol.* 21 (2022) 3357–3370.
- [16] C.D. Dai, T.L. Zhao, C.W. Du, et al., Effect of molybdenum content on the microstructure and corrosion behavior of FeCoCrNiMo high-entropy alloys, *J. Mater. Sci. Technol.* 46 (2019) 64–73.
- [17] C. Cui, M. Wu, R. He, et al., Effect of LaB₆ doping on the microstructure, microhardness and corrosion behavior of laser cladded FeCoNiCrMo coating on Ti6Al4V, *Surf. Coat. Tech.* 466 (2023) 129592.
- [18] A.A. Siddiqui, A.K. Dubey, Recent trends in laser cladding and surface alloying, *Opt. Laser Technol.* 134 (2021) 106619.
- [19] A. Vyas, J. Menghani, Parametric investigation of laser assisted cladding process: a review, *Mater. Today: Proc.* 44 (2021) 1828–1832.
- [20] F. Weng, H. Yu, C. Chen, et al., Effect of process parameters on the microstructure evolution and wear property of the laser cladding coatings on Ti-6Al-4V alloy, *J. Alloy. Compd.* 692 (2017) 989–996.
- [21] Y.P. Sun, Z. Wang, H.I. Yang, et al., Effects of the element La on the corrosion properties of CrMnFeNi high entropy alloys, *J. Alloys Compd.* 842 (2020) 155825.

- [22] M.L. Wang, H.Z. Cui, Y.Q. Zhao, et al., A simple strategy for fabrication of an FCC-based complex concentrated alloy coating with hierarchical nanoprecipitates and enhanced mechanical properties, *Mater. Des.* 180 (2019) 107893.
- [23] M.L. Wang, G.J. Zhang, H.Z. Cui, et al., Effect of plasma remelting on microstructure and properties of a CoCrCuNiAl0.5high-entropy alloy prepared by spark plasma sintering, *J. Mater. Sci.* 56 (2021) 5878–5898.
- [24] M. Li, B. Han, Y. Wang, et al., Effects of La₂O₃ on the microstructure and property of laser cladding Ni-based ceramic coating, *Optik* 130 (2017) 1032–1037.
- [25] P. Farahmand, T. Frosell, M. McGregor, et al., Comparative study of the slurry erosion behavior of laser cladded Ni-WC coating modified by nanocrystalline WC and La₂O₃, *Int. J. Adv. Manuf. Technol.* 79 (9) (2015) 1607–1621.
- [26] A.K. Das, Effect of rare earth oxide additive in coating deposited by laser cladding: a review, *Mater. Today: Proceed.* 52 (2022) 1558–1564.
- [27] S.M. AnilKuma Das, A.R. Shariff, Effect of rare earth oxide(Y₂O₃) addition on alloyed layer synthesized on Ti-6Al-4V substrate with Ti+SiC+h-BN mixed precursor by laser surface engineering, *Tribol. Int.* 95 (2016) 35–43.
- [28] Y. Feng, K. Feng, C. Yao, et al., Effect of LaB₆ addition on the microstructure and properties of (Ti₃Al + TiB)/Ti composites by laser cladding, *Mater. Des.* 181 (2019) 107959.
- [29] N. Zhang, X. Han, D. Sun, et al., Microstructure evolution and mechanical properties of La₆-modified Ti₂AlNb alloy fabricated by blended elemental powder metallurgy, *Powder Technol.* 369 (2020) 334–344.
- [30] I. Turkmen, K. Kanbur, F. Sargin, Characteristics of boronized Ti6Al4V alloy using boric acid based boronizing mixture, *Mater. Charact.* 192 (2022) 112180.
- [31] J. Liang, X. Yin, Z. Lin, et al., Effects of LaB₆ on microstructure evolution and properties of in-situ synthetic TiC+ TiBx reinforced titanium matrix composite coatings prepared by laser cladding, *Surf. Coat. Tech.* 403 (2020) 126409.
- [32] A. Enamian, S.F. Corbin, A. Khajepour, Effect of laser cladding process parameters on clad quality and in-situ formed microstructure of Fe-TiC composite coatings, *Surf. Coat. Tech.* 205 (7) (2010) 2007–2015.
- [33] D.D. Jie, M.P. Wu, R. He, et al., A multiphase modeling for investigating temperature history, flow field and solidification microstructure evolution of FeCoNiCrTi coating by laser cladding, *Opt. Laser Technol.* 169 (2024) 110197.
- [34] X. Zhang, H. Chen, L. Xu, et al., Cracking mechanism and susceptibility of laser melting deposited Inconel 738 superalloy, *Mater. Des.* 183 (2019) 108105.
- [35] E. Chauvet, P. Kontis, E.A. Jägle, et al., Hot crackingmechanism affecting a non-weldable Ni-based superalloy produced by selectiveelectron Beam Melting, *Acta Mater.* 142 (2018) 82–94.
- [36] Y.N. Liu, R.L. Sun, W. Niu, et al., Effects of CeO₂ on microstructure and properties of TiC/Ti₂Ni reinforced Ti-based laser cladding composite coatings, *Opt. Laser Eng.* 120 (2019) 84–94.
- [37] C. Wang, Y. Gao, R. Wang, et al., Microstructure of laser-clad Ni60 cladding layers added with different amounts of rare-earth oxides on 6063 Al alloys, *J. Alloys Compd.* 740 (2018) 1099–1107.
- [38] Z. Zhang, Y. Huang, A.R. Kasinathan, et al., 3-Dimensional heat transfer modeling for laser powder-bed fusion additive manufacturing with volumetric heat sources based on varied thermal conductivity and absorptivity, *Opt. Laser Technol.* 109 (2019) 297–312.
- [39] T.S. Wang, W.Y. Shi, Influence of substrate temperature on Marangoni convection instabilities in a sessile droplet evaporating at constant contact line mode, *Int. J. Heat Mass Transf.* 13 (2019) 1270–1278.
- [40] M. Alizadeh-Sh, S.P.H. Marashi, E. Ranjbarnodeh, et al., Laser cladding of Inconel 718 powder on a non-weldable substrate: clad bead geometry-solidification cracking relationship, *J. Manuf. Process.* 56 (2020) 54–62.
- [41] C. Limmaneevichitr, S. Kou, Experiments to simulate effect of arangoni convection on weld pool shape, *Weld J.* 79 (8) (2000) 231S–S237.
- [42] J. Hofman, D. De Lange, B. Pathiraj, et al., FEM modeling and experimental verification for dilution control in laser cladding, *J. Mater. Process. Technol.* 211 (2) (2011) 187–196.
- [43] V. Ocelík, U. de Oliveira, M. de Boer, et al., Thick co-based coating on cast iron by side laser cladding: analysis of processing conditions and coating properties, *Surf. Coat. Tech.* 201 (12) (2007) 5875–5883.
- [44] K. Wang, Q. Zhang, M. Sun, et al., Microstructure and corrosion resistance of laser clad coatings with rare earth elements, *Corros. Sci.* 43 (2) (2001) 255–267.
- [45] Y. Fu, C. Huang, C.W. Du, et al., Evolution in microstructure, wear, corrosion, and tribocorrosion behavior of Mo-containing high-entropy alloy coatings fabricated by laser cladding, *Corros. Sci.* 191 (2021) 109727.
- [46] I. Barin, F. Sauer, E. Schultze-Rhonhof, et al., Thermochemical data of pure substances, SERBULA (Sistema Librum 2.0) (1993) 1.
- [47] P. Wang, J. Li, C. Lin, et al., First-principles calculations of electronic structure and mechanical properties of Ti-Ni intermetallic compounds, *Chin. J. Nonferr. Metals* 26 (12) (2016) 2546–2554.
- [48] S.N.R. Abadi, Y. Mi, A. Kisielewicz, F. Sikström, et al., Influence of laser-wire interaction on heat and metal transfer in directed energy deposition, *Int. J. Heat Mass Tran.* 205 (2023) 123894.
- [49] L. Chen, Y. Zhao, B. Song, et al., Modeling and simulation of 3D geometry prediction and dynamic solidification behavior of Fe-based coatings by laser cladding, *Opt. Laser Technol.* 139 (2021) 107009.
- [50] Y. Cao, N. Farouk, M. Taheri, et al., Evolution of solidification and microstructure in laser-clad IN625 superalloy powder on GTD-111 superalloy, *Surf. Coat. Tech.* 412 (2021) 127010.
- [51] L. Chen, T. Yu, P. Xu, et al., In-situ NbC reinforced Fe-based coating by laser cladding: Simulation and experiment, *Surf. Coat. Tech.* 412 (2021) 127027.
- [52] Z. Chen, M. Taheri, The effect of pre-heating and pre-cold treatment on the formation of liquation and solidification cracks of nickel-based superalloy welded by laser beam, *J. Mater. Res. Technol.* 9 (2020) 11162–11177.
- [53] S.B. Park, Heterogeneous nucleation models to predict grain size in solidification, *Prog. Mater. Sci.* 123 (2022) 100822.
- [54] C.V. Rao, G.M. Reddy, K.S. Rao, Microstructure and pitting corrosion resistance of AA2219 Al-Cu alloy friction stir welds effect of tool profile, *Def. Technol.* 11 (2) (2015) 123–131.
- [55] Z. Gao, L. Wang, Y. Wang, et al., Crack defects and formation mechanism of FeCoCrNi high entropy alloy coating on TC4 titanium alloy prepared by laser cladding, *J. Alloys Compd.* 903 (2022) 163905.
- [56] R. Song, J. Li, J.Z. Shao, et al., Microstructural evolution and wear behaviors of laser cladding Ti2Ni/ α (Ti) dual-phase coating reinforced by TiB and TiC, *Appl. Surf. Sci.* 355 (2015) 298–309.
- [57] Y. Lin, J. Yao, Y. Lei, et al., Microstructure and properties of TiB₂–TiB reinforced titanium matrix composite coating by laser cladding, *Opt. Laser Eng.* 86 (2016) 216–227.
- [58] N. Hansen, Hall-Petch relation and boundary strengthening, *Scr. Mater.* 51 (2004) 801–806.
- [59] H. Van Swygenhoven, P.M. Derlet, A. Hasnaoui, Atomic mechanism for dislocation emission from nanosized grain boundaries, *Phys. Rev. B* 66 (2) (2002) 024101.
- [60] X.L. Zhang, Z.H. Jiang, Z.P. Yao, et al., Effects of scan rate on the potentiodynamic polarization curve obtained to determine the Tafel slopes and corrosion current density, *Corros. Sci.* 51 (3) (2009) 581–587.
- [61] X. Guozhi, S. Xiaolong, Z. Dongjie, et al., Microstructure and corrosion properties of thick WC composite coating formed by plasma cladding, *Appl. Surf. Sci.* 256 (21) (2010) 6354–6358.
- [62] F.M. Shen, W. Tao, L.Q. Li, et al., Effect of microstructure on the corrosion resistance of coatings by extreme high speed laser cladding, *Appl. Surf. Sci.* 517 (2020) 146085.
- [63] T. Okada, Pit nucleation originated by coupling of perturbations with local anodic sites on passive metals, *Electrochim. Acta* 33 (1988) 389–395.
- [64] Y. Shi, B. Yang, X. Xie, et al., Corrosion of Al_xCoCrFeNi high-entropy alloys: Al-content and potential scan-rate dependent pitting behavior, *Corros. Sci.* 119 (2017) 33–45.
- [65] F. Rosalbino, D. Maccio, G. Scavino, et al., In vitro corrosion behaviour of Ti–Nb–Sn shape memory alloys in Ringer's physiological solution, *J. Mater. Sci.-Mater. m.* 23 (2012) 865–871.
- [66] H. Luo, M. Leitch, Y. Behnamian, et al., Development of electroless Ni–P/nano-WC composite coatings and investigation on its properties, *Surf. Coat. Tech.* 277 (2015) 99–106.
- [67] W. Wang, A. Alfantazi, Effect of microstructure and temperature on electrochemical behavior of niobium in phosphate-buffered saline solutions, *J. Electrochem. Soc.* 160 (1) (2012) C1.
- [68] S. Ahn, H. Kwon, Diffusivity of point defects in the passive film on Fe, *J. Electroanal. Chem.* 579 (2) (2005) 311–319.
- [69] Z. Cui, L. Wang, H. Ni, et al., Influence of temperature on the electrochemical and passivation behavior of 2507 super duplex stainless steel in simulated desulfurized flue gas condensates, *Corros. Sci.* 118 (2017) 31–48.
- [70] X. Wen, Z. Cai, B. Yin, et al., Tribological and corrosion properties of Ni-Cr-Co-Ti-V multi-principal element alloy prepared by vacuum hot-pressing sintering, *Adv. Eng. Mater.* 21 (7) (2019) 1801239.
- [71] E. Sikora, J. Sikora, D.D. Macdonald, A new method for estimating the diffusivities of vacancies in passive films, *Electrochim. Acta* 41 (6) (1996) 783–789.
- [72] D.D. Macdonald, The point defect model for the passive state, *J. Electrochem. Soc.* 12 (1992) 3434–3449.
- [73] M.E. Orazem, I. Frateur, B. Trbolet, et al., Dielectric properties of materials showing constant-phase-element (CPE) impedance response, *J. Electrochem. Soc.* 160 (6) (2013) C215.
- [74] D. Jiang, H.Z. Cui, H. Chen, et al., Wear and corrosion properties of B4C-added CoCrNiMo high-entropy alloy coatings with in-situ coherent ceramic, *Mater. Des.* 58 (2021) 110068.